

## Article

# Experimental Thermohydraulic Assessment of Novel Curved Ribs for Heat Exchanger Tubes: A Machine Learning Approach

Prashant Deshmukh <sup>1</sup>, Subhash Lahane <sup>2</sup>, Hari Sumant <sup>3</sup>, Abhishek D. Patange <sup>1,\*</sup>  
and Sakthivel Gnanasekaran <sup>4</sup>

<sup>1</sup> Department of Mechanical Engineering, COEP Technological University, Pune 411005, India

<sup>2</sup> Department of Mechanical Engineering, Deogiri Institute of Engineering and Management Studies, Aurangabad 431005, India

<sup>3</sup> School of Computer Science and Engineering, Vellore Institute of Technology, Bhopal 466114, India

<sup>4</sup> School of Mechanical Engineering, Vellore Institute of Technology, Chennai 600127, India

\* Correspondence: abhipatange93@gmail.com

**Abstract:** Heat transfer enhancement using curved ribs of different cross sections, viz., square, rectangular, triangular, and circular, is a crucial study for designing heat-exchanging devices for various applications, and their thermohydraulic performance prediction using machine learning technique is a vital part of the modern world. An experimental study on using curved ribs suitable for heat transfer enhancement for the circular tube is presented for turbulent airflow with Reynolds numbers varying from 10,000 to 50,000. The machine learning methodology is used to predict the thermohydraulic performance assessment of curved ribs. The square cross-sectioned curved ribs produce the highest performance factor  $R3$  of 1.5 to 2.65 to the equivalent Reynolds number  $Rec$  value of 20,000. It is observed that most of the curved rib configurations show a performance ratio  $R3$  maximum and are suitable at a low Reynolds number value. At moderate and high Reynolds number values, the performance factor values decrease due to a rise in the pressure drop values for a few curved rib configurations. An artificial neural network (ANN) model predicts with an accuracy of 95% with the present study experimental values for the heat transfer performance indicators like average heat transfer enhancement  $Nua/Nus$ , average heat transfer enhancement  $fa/fs$ , and performance ratio  $R3$ , i.e.,  $Nua/Nuc$ .

**Keywords:** heat transfer augmentation; turbulent flow; rib; machine learning; prediction



**Citation:** Deshmukh, P.; Lahane, S.; Sumant, H.; Patange, A.D.; Gnanasekaran, S. Experimental Thermohydraulic Assessment of Novel Curved Ribs for Heat Exchanger Tubes: A Machine Learning Approach. *Aerospace* **2023**, *10*, 658. <https://doi.org/10.3390/aerospace10070658>

Academic Editor: Jian Liu

Received: 10 June 2023

Revised: 10 July 2023

Accepted: 17 July 2023

Published: 24 July 2023



**Copyright:** © 2023 by the authors. Licensee MDPI, Basel, Switzerland. This article is an open access article distributed under the terms and conditions of the Creative Commons Attribution (CC BY) license (<https://creativecommons.org/licenses/by/4.0/>).

## 1. Introduction

Heat transfer enhancement plays a vital role in the initial design of heat-exchanging devices for electrical, electronics, industrial plants, refrigeration, solar heaters, turbines, air conditioning, and therapeutic purposes. Most of the methods for enhancing heat transfer in existing heat exchanger systems are inclined towards better fluid mixing, thereby improving heat transfer efficiency in different types of applications like conversion of liquid to vapour [1,2] and low droplet impact cooling [3–5]. The various passive heat transfer enhancement methods are ribs and impingement [6,7], vortex generators [8], the usage of numerous microchannels [9,10], small pin fins [11] and conventional twisted tapes [12]. These techniques cause rapid fluid mixing between cold and hot regions in the flow sections, further causing higher heat transfer. Miniature pin-fin heat dissipation is used in high-level heat-flux electronic applications, as it helps in enhancing heat transfer. They are also used for flow blending, necessitating comparatively small pumping power than traditional microchannel heat sinks. Interestingly, the rib components can also perform the role of tiny fins [12], which further enhances the heat by conduction mode. An enhancement in the slot width-to-rib height proportion tends to separate the jet from the rib to reattach again for the next stage and circulate within the cavity. These flow alterations reconnect, and the flow's recirculation considerably enhances heat transfer.

Another factor that considerably augments the heat transfer is the roughness of the heat-exchanging surface owing to increased turbulence intensity of flow near the surface, which further adds intense fluid mixing. Ribs are passive augmentation devices that also contribute to heat transfer augmentation as they act as surface turbulators [13]. The heat transmission can be increased by broken V-ribbed twisted tapes (B-VRTs) [14] for better blending, instigated by the longitudinal waterspouts from the ribs and swirling stream from the distorted tape. The B-VRT with different rib angles was verified using air. The comparative analysis of the tube with B-VRTs in the arrangement of forward and backward with a flat tube and a tube with distorted tapes were carried out for 6000 and 20,000 Reynolds numbers. The developed correlations for the Nusselt number and friction factor for estimating heat transfer rate and drop in pressure showed acceptable prediction accuracies [14]. However, the accurate correlations did not predict the multidimensional, nonlinear function correlation among variables in heat transfer applications [15]. The impacts of rib heights, pitch and flow paths, fluid structure, and behaviour are studied within a laminar flow regime. Numerical analysis was used to foresee the fluid structure and thermal behaviour within the ribbed duct [16]. It was observed that rib height significantly affects the flow and heat transfer behaviour.

Machine learning (ML) has played a vital role in different applications since 1950, when Arthur Samuel [17] conceptualised it for the first time. Rosenblatt invented the perceptron [18], and Werbos invented a multistratified perceptron [19] in 1974. Initially, ML was used for straightforward interpretations, such as understanding the conventions in a game of supervisors [20] and identifying arrangements [21]. Subsequently, with the advancement of information technology and several ML processes, encompassing support vector machines, boosting processes, and collaborative learning, ML has been used in numerous applications like genetics and genomics, computer engineering, environmental science, industrial, healthcare, and banking and economics. ML has the numerous merits of being proficient at artificially learning the complicated association between dependent and independent variables with high precision. Thus, its application is enthusiastically found in research related to thermal and fluid engineering. A few papers that consider ML-based techniques for heat transfer augmentation are reviewed. The hybrid approach for heat transfer enhancement using computational fluid dynamics and artificial neural networks was implemented. An artificial neural network (ANN) was implemented to find optimum rib roughness due to low computational cost and prediction error of less than 1.5% [22]. The random forest algorithm was used to predict the convection heat transfer coefficients for a cooling channel unified with adjustable rib coarseness [23]. Kim et al. [10] established universal machine learning standards for forecasting the thermal presentation of miniature pin-fin heat dissipation of different structures and under different working circumstances beyond the constraints of functional relationships by employing power law regression. Heat transfer was investigated for a double-layered microchannel heat sink with wavy and porous ribs. The authors indicate the 'holdout method' for the generalised accuracy of the model. The prediction accuracy for different test models ranged from 87.45% to 93.51%. The CNN intelligent agent cloud architecture was employed to verify errors in reading medical image data. In the present study, an artificial neural network (ANN) model was used for predicting experimental results of heat transfer and pressure drop. An attempt was made to predict these data using different methodologies like ANN or CNN. ANN was used to optimise the performance and impact of wavy and porous ribs on the Nusselt number, pressure drop, and temperature difference [24,25]. ML algorithms were implemented to model heat transfer correlations, such as the Nusselt number and friction factor for a heat exchanger with distorted tape inserts. The data-driven substitute modelling employed polynomial regression, random forest, and artificial neural networks. It is noted that the ANN estimation of heat transfer coefficients surpasses the estimations of P.R. and R.F. across different test datasets [26]. ML tools considerably diminish the attempt to build multivariable heat transfer relationships. Therefore, it is necessary to implement the machine learning algorithm for the complex heat transfer system.

It is important to note here that abundant passive techniques are available for heat transfer enhancement for single-phase heat transfer using ribs. These passive techniques for enhancing heat transfer were reported to be used for flow through square/rectangular cross sections; however, their use in enhancing heat transfer for the flow through circular geometries is not yet reported. Hence, in the present study, an attempt was made to capture the potential of ribs. The customisation in the shape of the straight ribs into curved-shaped ribs was introduced so as to make them a suitable tool for enhancing heat transfer in circular tubes. The thermohydraulic performance prediction needs to be carried out using a machine learning tool. Results of this study will assist researchers in this domain of single-phase heat transfer augmentation to predict the thermodynamic performance based on the sophisticated ML-based methodology. An experimental study on using curved ribs suitable for heat transfer enhancement for the circular tube is presented for turbulent airflow with Reynolds numbers varying from 10,000 to 50,000. The machine learning methodology is used to predict the thermohydraulic performance assessment of curved ribs. The square cross-sectioned curved ribs produce the highest performance factor  $R3$  of 1.5 to 2.65 to the equivalent Reynolds number  $Rec$  value of 20,000. It is observed that most of the curved rib configurations show a performance ratio  $R3$  maximum and are suitable at a low Reynolds number value. At moderate and high Reynolds number values, the performance factor values decrease due to a rise in the pressure drop values for a few curved rib configurations. In the present study, an artificial neural network (ANN) model predicts with an accuracy of 95% the experimental values for the heat transfer performance indicators, such as average heat transfer enhancement,  $Nua/Nus$ , average heat transfer enhancement,  $fa/fs$ , and performance ratio  $R3$ , i.e.,  $Nua/Nuc$ .

## 2. Experimentation and Data Collection

This section describes the experimental setup for measuring the average Nusselt number and friction factor. The experimental setup, validation, and data reduction details are presented. The experimental procedure is discussed to obtain the average heat transfer and pressure drop data. Heat transfer and pressure drop results for turbulent flow through an empty tube are matched with the standard relations specified by Dittus and Boelter [27].

### 2.1. Experimental Setup

An experimental setup was built to determine average heat transfer using curved ribs and a smooth tube. Figure 1 indicates the assembly of the test system used. Figure 2 shows the sketch of the test section used to measure average heat transfer. The test tube is 1000 mm long and made of stainless steel with inner and outer diameters of 24.50 and 25 mm, respectively. Two copper flanges are soldered at the end of the test section. Three 50 mm long copper sleeves are soldered on the steel tube at a regular interval of 270 mm. Copper sleeves are used to minimise the circumferential variation in temperature that occurs due to the inserts. Three calibrated Chromel–Alumel K-type thermocouples are soldered at 120 degrees tangentially and 2.5 mm axially apart on each copper sleeve to measure its surface temperature. To provide uniform heat flux, nichrome wire is covered over the perimeter of the test tube from the inlet flange to the exit flange. The tube, copper flanges, and exit sections are insulated using ceramic wool to minimise heat loss. Air as the test fluid is pushed into the test tube using an air compressor. The airflow in the test tube is controlled using a regulator and a bypass valve. The differential pressure head across calibrated venturimeter is given by U tube water, and a mercury manometer is used for measurement of the mass flow rate of air. The exit of the test section is a 500 mm long thermally insulated mild steel pipe. Three calibrated Chromel–Alumel K-type thermocouples measure the bulk temperature of the airflow in the test section. Three thermocouples at different radial directions, each at the exit and entry of the test section, are used to measure the bulk mean air temperature. An Agilent data acquisition system (34970A) is used to measure and store the voltage across the two junctions of the thermocouples. Four pressure taps at an angle of 90° to each other are attached to the

pipe at the entry section, 50 mm upstream from the inlet flange. One end of the U-tube manometer is attached to this pressure tap. A similar pressure tap is attached to the pipe 150 mm downstream from the outlet flange. The other end of the U-tube manometer is attached to this pressure tap to find the pressure drop across the tube. A U-tube water manometer shows the pressure difference across the test tube and the venturimeter. A water manometer is used at low flow rates ( $Re$  range 10,000 to 25,000), whereas mercury is utilised as a manometric fluid at higher flow rates ( $Re$  range 35,000 to 55,000).

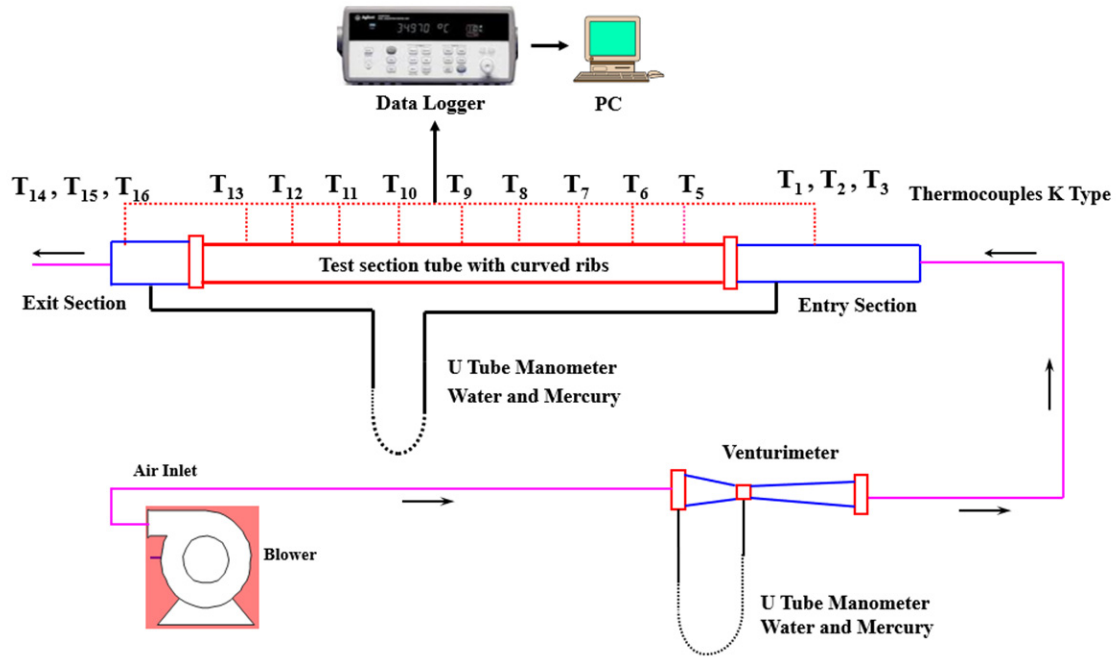


Figure 1. Schematic of the experimental test setup.

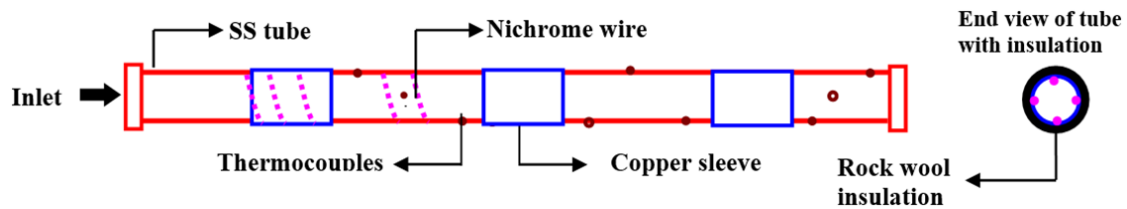


Figure 2. Schematic of the test section.

### 2.2. Experimental Procedure and Data Reduction

Test fluid air is allowed to flow through the test section. The globe valve adjusts the mass flow rate of air to provide the desired Reynolds number at the inlet of the test tube. The variable transformer provides the test tube’s entire periphery with constant heat flux. The wall, inlet, and outlet temperature readings are recorded at a steady state. The average Nusselt number is the mean of the Nusselt number obtained from individual sleeves. The friction factor is calculated in terms of pressure drop measured by the U-tube manometer.

The friction factor is determined as follows:

$$f = \frac{\pi^2 \times \Delta p \times d^5 \times \rho}{32 \times L \times \dot{m}^2} \tag{1}$$

This friction factor is compared with the following expression given by Blasius [27] for fully developed turbulent flow in a smooth tube ( $10^4 < Re < 10^6$ ):

$$f_s = 0.079 \times Re^{-0.25} \tag{2}$$

The power distributed to the test tube is determined by measuring the electrical current  $I$  and voltage  $V$ .

$$Q_{in} = I \times V \quad (3)$$

The heat taken by the air during its flow through the test tube is

$$Q_{out} = \dot{m} \times C_p \times (T_{bo} - T_{bi}) \quad (4)$$

The outlet and inlet air temperatures  $T_{bo}$  and  $T_{bi}$  are calculated using the temperature readings from three thermocouples at the inlet and outlet of the test tube. The energy imbalance  $Q_{imbalance}$  is calculated as:

$$Q_{imbalance} = Q_{in} - Q_{out} \quad (5)$$

The energy input given to the system is the electrical power, specified in Equation (3), and the heat energy taken away by the flowing fluid while its travel from inlet to outlet is specified by Equation (4). The mismatch between  $Q_{in}$  and  $Q_{out}$  is observed to be always less than 10% of total electrical energy input to the system. This value is observed to be consistently less than 10% for all the experimental test runs. This variance is due to the uncertainties in the measurement of voltage, electrical current, temperature of the wall, temperature of the fluid at inlet and outlet conditions, and the flow rates of fluid at the inlet.

The bulk temperature is expected to vary in a linear manner throughout the test tube, beginning from the inlet to the outlet. The intermediary values are taken by interpolation between the temperatures recorded for the inlet to outlet bulk temperatures. The average value of the Nusselt number for a completely established flow is defined as follows:

$$Nu_{avg} = \frac{Q_{out} \times d}{A(T_{wavg} - T_{bavg})k} \quad (6)$$

The Nusselt number for the smooth tube is achieved by utilising the Dittus–Boelter equation:

$$Nu_s = 0.023 \times Re^{0.8} \times Pr^{0.4} \quad (7)$$

The power required to pump the augmented tube is more due to the considerable frictional opposition to the fluid flow than the smooth tube. Running the smooth tube at a high Reynolds number is necessary to compare the augmented tube with the smooth tube at a similar pumping power. This high Reynolds number is stated here as equivalent Reynolds number  $Re_c$ , and it can be determined by comparison of the pumping power between the augmented tube and the smooth tube.

$$(Re_a)^3 \cdot f_a = (Re_c)^3 \cdot f_c \quad (8)$$

$Re_a$  and  $Re_c$  are the augmented-case Reynolds number and equivalent Reynolds number for smooth tubes at the same pumping power. The terms  $f_c$  and  $f_a$  are the equivalent smooth-tube friction factor and enhanced-case friction factor at the same pressure drop, i.e., equal pumping power. Using the Blasius equation [27], the friction factor for smooth-tube turbulent flow conditions,

$$f_c = \frac{0.079}{Re_c^{0.25}} \quad (9)$$

and Equation (8) gives

$$Re_c = \left[ f_a \times \frac{Re_a^3}{0.079} \right]^{0.3636} \quad (10)$$

The value of  $Nu_c$  for the empty tube is evaluated at this equivalent Reynolds number,  $Re_c$ , using Equation (7); the assessment criterion  $R3$  is defined as:

$$R3 = \frac{Nu_a}{Nu_c} \quad (11)$$

The uncertainty in the measurement of experimental values of pressure and temperature were discovered to be  $\pm 0.1$  kPa and  $\pm 0.33$  °C, respectively. The root-mean-square (RMS) uncertainty of the average heat transfer coefficient and friction factor was determined using the uncertainties in the measured data given by Moffat [28] and found to be 14.48% and 9.46%, respectively.

### 2.3. Experimental Data Validation Using a Tube Retrofitted with a Helical Wire Coil (HWC)

The experimental test facility is validated using a tube installed with an HWC. The heat transfer and pressure drop data for the tube fitted with HWC inserts have been extensively studied and reported in the literature. An experimental study is performed for the HWC to validate the experimental setup. The results are compared with the correlation specified by Garcia et al. [29] (2005) and Zhang et al. [30] (1991). The parameters of the HWC that influence the heat transfer performances are height-to-diameter ratio ( $e/d$ ), pitch-to-height ratio ( $p/e$ ), helical angle  $\alpha$ , and Reynolds number, as stated in Table 1. Therefore, the Nusselt number and friction factor can be expressed as  $Nu = \varphi(p/e, e/d, Re)$  and  $f = \varphi(p/e, e/d, Re)$ .

The experiments are carried out on Reynolds numbers based on the hydraulic diameter of the test section and vary in the range 10,000–55,000. The results for average heat transfer enhancement and friction loss in the tube with helical wire coil insert ( $p/d = 1.18$ ,  $p/e = 12.0$ , and  $e/d = 0.1$ ) at various Reynolds numbers are shown in Figures 3 and 4, respectively. Figure 4 indicates that the present study has a difference of 6 to 11% and 1 to 5% in the values of the Nusselt number with estimates specified by Garcia et al. [29] and Zhang et al. [30], respectively. The variation in the measurement of pressure drop is 2 to 5% and 0.3 to 16% with values specified by Garcia et al. [29] and Zhang et al. [30] respectively as shown in Figure 4. Figures 3–5 show that the values specified by the investigators Garcia et al. [29] and Zhang et al. [30] agree well with the present experimentally obtained values for pressure drop and Nusselt numbers.

**Table 1.** Geometry parameters of helical wire coil.

Parameter	Range
Axial pitch	30 mm
Height of roughness, $e$	2.5 mm
Helical angle, $\alpha$	$45^\circ$
Reynolds number, $Re$	10,000–55,000

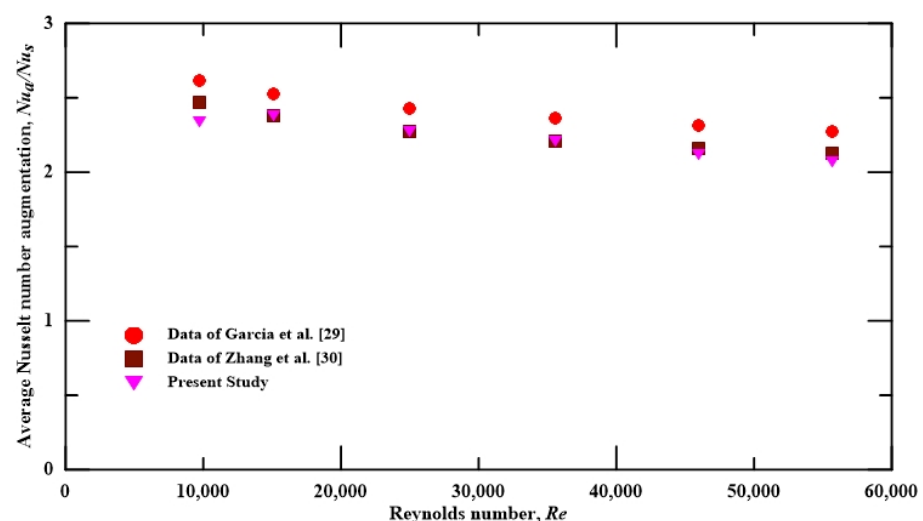


**Figure 3.** Average  $Nu/Nu_s$  v/s Reynolds number for helical wire coil having  $p/d = 1.18$ ,  $p/e = 12$ , and  $e/d = 0.1$ .

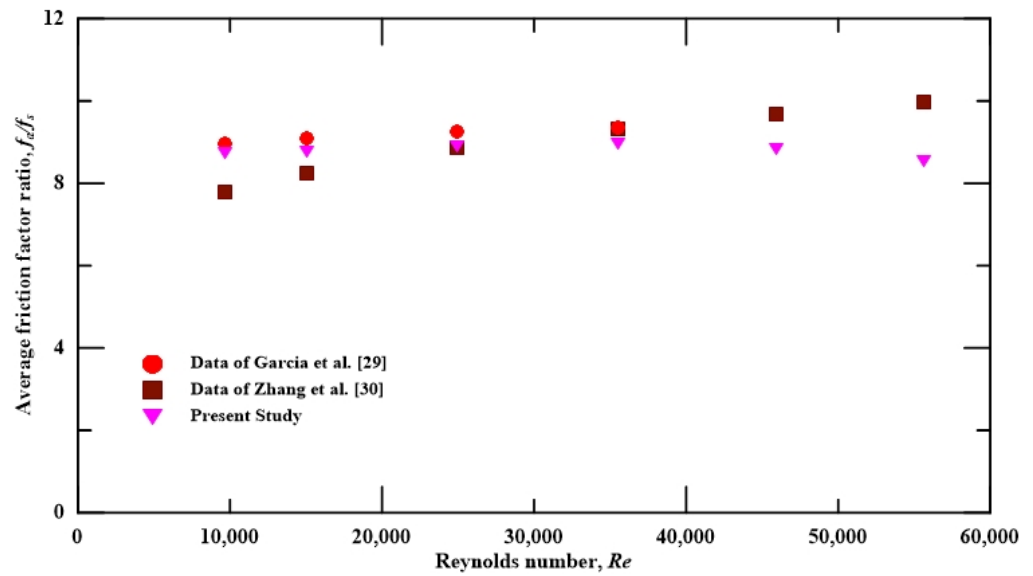


**Figure 4.** Average  $f_d/f_s$  v/s Reynolds number for helical wire coil having  $p/d = 1.18$ ,  $e/d = 0.1$ , and  $p/e = 12$ .

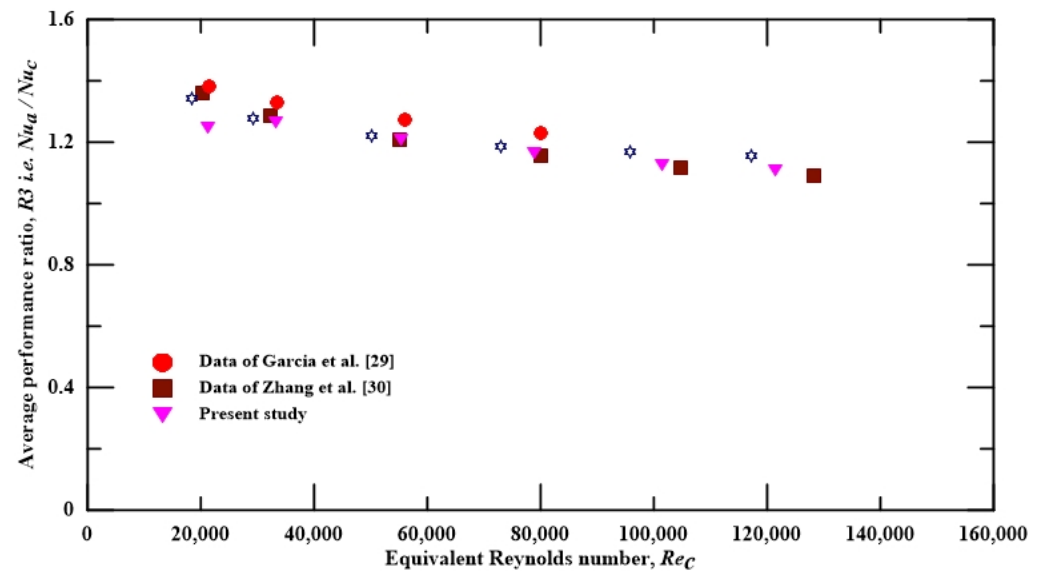


**Figure 5.** Average  $Nu_d/Nu_c$  v/s Reynolds number for helical wire coil having  $p/d = 1.18$ ,  $e/d = 0.1$ , and  $p/e = 12$ .

#### 2.4. Data Representation

The geometry of the curved rib, shown in Figure 6, is a cross-section of different shapes, viz., square, rectangle, equilateral triangle, circle of thickness  $b$ , and height  $e$ , including angle  $\alpha$ . The outer portion of the curved rib element is first attached to the inner wall of the tube. The height  $e$  specifies the roughness height of the tube, as this dimension of the curved rib extends in the path perpendicular to the flow. The included angle  $\alpha$  specifies that the rib length in the radial direction is a rough part of the tube in the circumferential direction. The geometrical dimensions of the curved ribs, as shown in Table 2, were aligned in a streamwise direction, as shown in Figure 7.

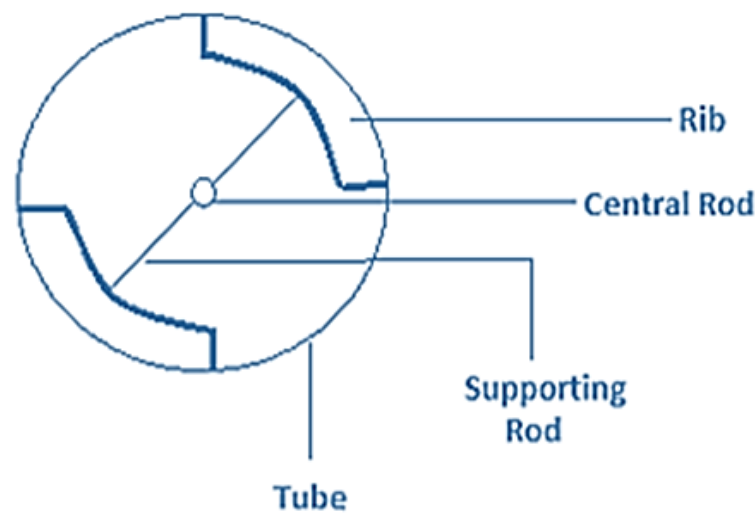
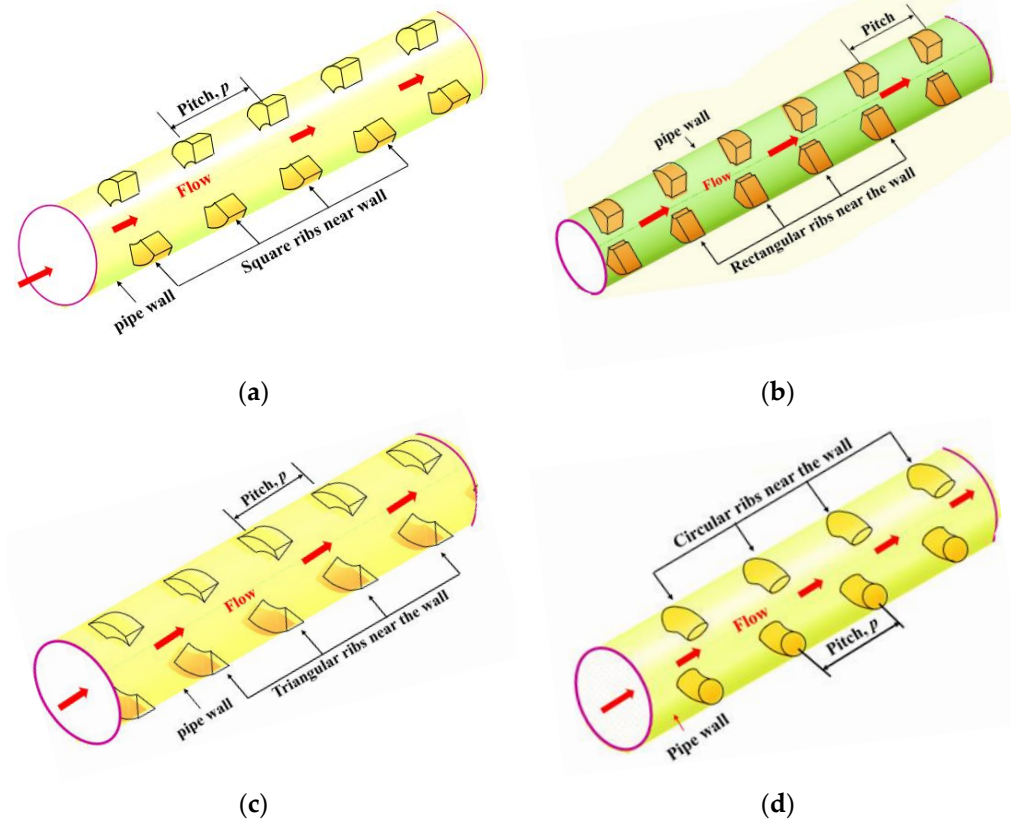


Figure 6. Cross-sectional view of a tube with curved rib.

Table 2. Dimensions of rib elements.

Rib Cross-Section	Contact Angle of the Rib, $\alpha$ ( $^{\circ}$ )	Rib Thickness $t$ (mm)	Rib Height, $e$ (mm)	Pitch to Rib Thickness Ratio, $p/t$ (-)	Rib Height to Inner Tube Diameter Ratio, $e/d$ (-)
Circle	45 $^{\circ}$	6	6	4.17	0.24
	45 $^{\circ}$	6	6	8.33	0.24
	45 $^{\circ}$	6	6	16.67	0.24
	45 $^{\circ}$ , 60 $^{\circ}$	9	9	2.78	0.35
	45 $^{\circ}$ , 60 $^{\circ}$	9	9	5.56	0.35
	45 $^{\circ}$ , 60 $^{\circ}$ , 90 $^{\circ}$	9	9	11.11	0.35
Rectangular	45 $^{\circ}$ , 60 $^{\circ}$ , 90 $^{\circ}$	3	6	33.33	0.24
	45 $^{\circ}$ , 60 $^{\circ}$ , 90 $^{\circ}$	3	9	33.33	0.35
	45 $^{\circ}$	6	9	4.17	0.35
	45 $^{\circ}$ , 60 $^{\circ}$	6	9	8.33	0.35
	45 $^{\circ}$ , 60 $^{\circ}$ , 90 $^{\circ}$	6	9	16.67	0.35
	45 $^{\circ}$	9	6	2.78	0.24
	45 $^{\circ}$ , 60 $^{\circ}$	9	6	5.56	0.24
Square	45 $^{\circ}$ , 60 $^{\circ}$ , 90 $^{\circ}$	9	6	11.11	0.24
	45 $^{\circ}$ , 60 $^{\circ}$ , 90 $^{\circ}$	3	3	33.33	0.12
	45 $^{\circ}$ , 60 $^{\circ}$ , 90 $^{\circ}$	6	6	16.67	0.24
	45 $^{\circ}$ , 60 $^{\circ}$ , 90 $^{\circ}$	9	9	11.11	0.35
	90 $^{\circ}$	6	6	4.17, 8.33	0.24
Equilateral triangle	45 $^{\circ}$ , 60 $^{\circ}$	6	5.2	4.17	0.2
	45 $^{\circ}$ , 60 $^{\circ}$	6	5.2	8.33	0.2
	45 $^{\circ}$ , 60 $^{\circ}$ , 90 $^{\circ}$	6	5.2	16.67	0.2
	45 $^{\circ}$	9	7.8	5.56	0.31
	45 $^{\circ}$	9	7.8	11.11	0.31

In the present study, experiments were performed on various configurations to reveal their thermohydraulic performance under different flow conditions at the inlet of the pipe, corresponding to Reynolds numbers ranging from 5000 to 50,000. The rib geometry of different configurations is shown in Table 2. The geometry details are presented in dimensionless forms, i.e., the ratio of the pitch to rib thickness  $p/t$  and the ratio of rib height to tube inner diameter  $e/d$ .



**Figure 7.** In-line arrangement of curved ribs of (a) square, (b) rectangle, (c) equilateral triangle, and (d) circle cross-section.

### 3. Experimental Results and Discussion

The thermal performance assessment parameters are discussed in this section; these include average heat transfer enhancement ratios  $Nu_a/Nu_s$ , average friction-factor ratios  $f_a/f_s$ , and average performance factor  $R3$ , i.e.,  $Nu_a/Nu_c$  for different configurations of rib elements comprising different  $p/t$  ratios, including angles  $\alpha$ , and  $e/d$  ratios.

#### Heat Transfer and Pressure Drop Results for Different Configurations

Figure 8 shows the thermal performance indicators like average heat transfer enhancement ratios  $Nu_a/Nu_s$ , average friction-factor ratios  $f_a/f_s$ , and average performance factor  $R3$ , that is,  $Nu_a/Nu_c$  for different configurations of square rib elements comprising different  $p/t$  ratios, including angles  $\alpha$  and  $e/d$  ratios, for square rib configuration. The average enhancement ratio  $Nu_a/Nu_s$ , is observed to be at a maximum for the square rib with a  $p/t$  ratio of 16.67, contact angle  $\alpha$  equal to  $90^\circ$ , and  $e/d$  ratio equal to 0.24, as indicated in Figure 8a. It is important to note that the configuration of the rib element, which involves a higher contact angle  $\alpha = 90^\circ$ , shows a higher enhancement factor. This enhancement is due to the higher contact of the rib element with the heated inner wall of the tube compared to the other rib configurations in which  $\alpha$  equals  $45^\circ$  and  $60^\circ$ . All configurations show an enhancement factor between 1.5 and 4.0 for Reynolds numbers up to 20,000; however, after this Re value, the enhancement gradually decreases to 1.0 for a few configurations. The variation in the friction-factor augmentation  $f_a/f_s$  with Reynolds number for different square rib configurations is shown in Figure 8b. It is observed that this ratio remains almost uniform with the variation in the Reynolds number. The average performance factor  $R3$ , i.e.,  $Nu_a/Nu_c$  for different configurations of square ribs comprising different  $p/t$  ratios, contact angles  $\alpha$ , and  $e/d$  ratios, is shown in Figure 8c. The average performance factor  $R3$  is observed to be the maximum for the square rib having a  $p/t$  ratio of 16.67, contact angle  $\alpha$  equal to  $90^\circ$ , and  $e/d$  ratio equal to 0.24.

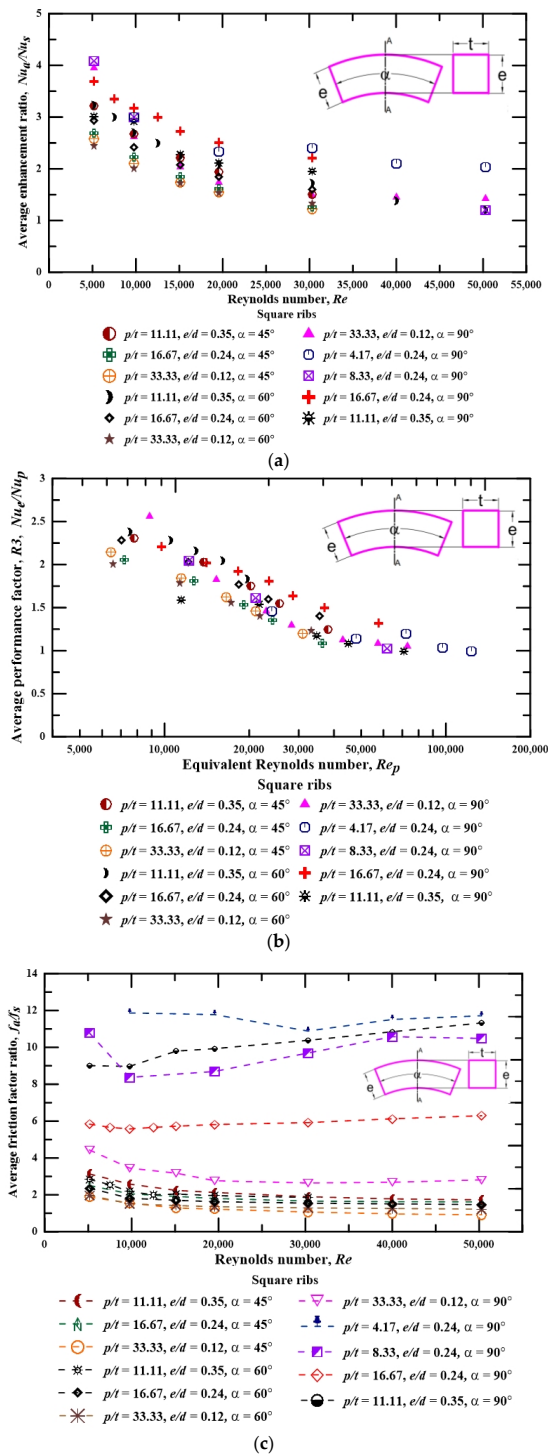


**Figure 8.** Experimental results for square ribs variation in (a) average enhancement ratio  $Nu_a/Nu_s$  with Reynolds number  $Re$ ; (b) average performance factor  $R3$ , i.e.,  $Nu_a/Nu_c$  with equivalent Reynolds number  $Re_c$ ; (c) average friction-factor ratio  $f_a/f_s$  with Reynolds number  $Re$ .

The variation in the average heat transfer enhancement ratio  $Nu_a/Nu_s$  with the Reynolds number for triangular and rectangular curved ribs is shown in Figures 9a and 10a, respectively. It is observed that the enhancement ratios are relatively higher until a Reynolds number equal to 20,000 is attained, after which the enhancement ratio decreases and remains almost constant with the Reynolds number. This observation is valid for all curved triangular and rectangular rib configurations. The variation in the friction-factor augmentation  $f_a/f_s$  with the Reynolds number for different square rib configurations are

shown in Figures 9b and 10b. It is concluded that the lower values of the  $p/t$  ratio equal to 4.17, in the case of triangular ribs, produce a significant pressure drop. In contrast, rectangular ribs produce more pressure drop at a higher contact angle  $\alpha$ , more than  $45^\circ$ . Figure 11c shows the average performance factor R3 for triangular ribs, and it is observed to be in the range 1.5 to 2.0 until the equivalent Reynolds number is equal to 20,000. However, in the case of the rectangular ribs, this value of the average performance factor R3 is relatively low compared to the triangular ribs, as shown in Figure 10c. Figure 11a shows the variation in the average heat transfer enhancement ratio  $Nua/Nus$  with the Reynolds number for the curved circular ribs. The configuration with the lowest  $p/t$  ratio of 2.78,  $e/d$  ratio = 0.35, and  $\alpha$  equal to  $60^\circ$  showed the maximum value of heat transfer enhancement. It should be noted that for a particular configuration of circular ribs, a constant value of heat transfer augmentation was observed at all values of the Reynolds number. This can be attributed to the maximum number of circular rib elements in the tube, which causes swirl intensification within the mainstream flow. Figure 11b shows the friction-factor enhancement ratio  $f_{a}/f_s$  variation with the Reynolds number for the circular ribs. It is observed that this ratio is observed to be the maximum for lower  $p/t$  ratio and higher contact angle  $\alpha$  configurations.

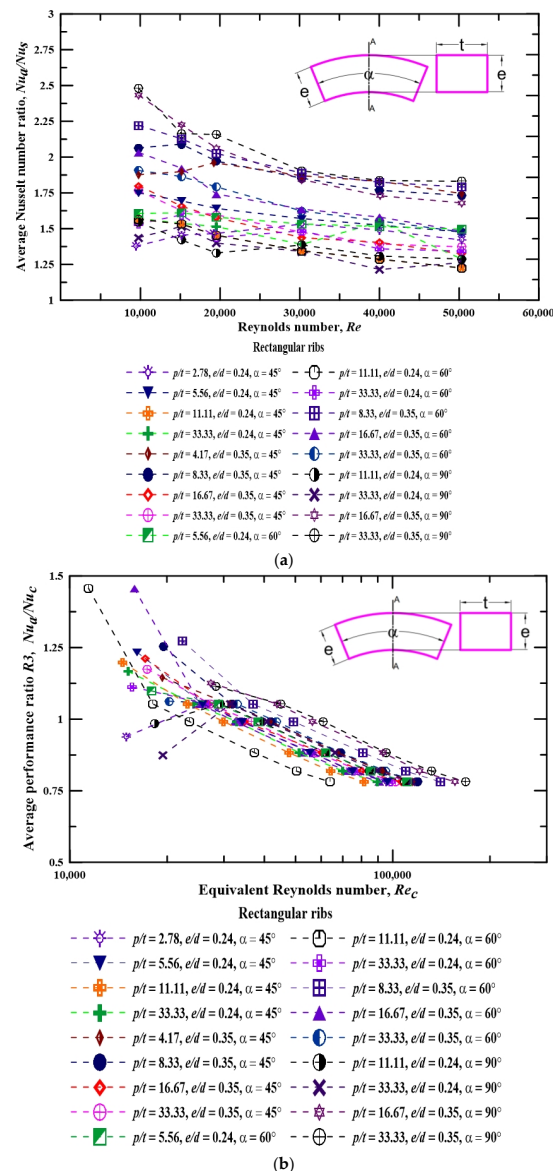
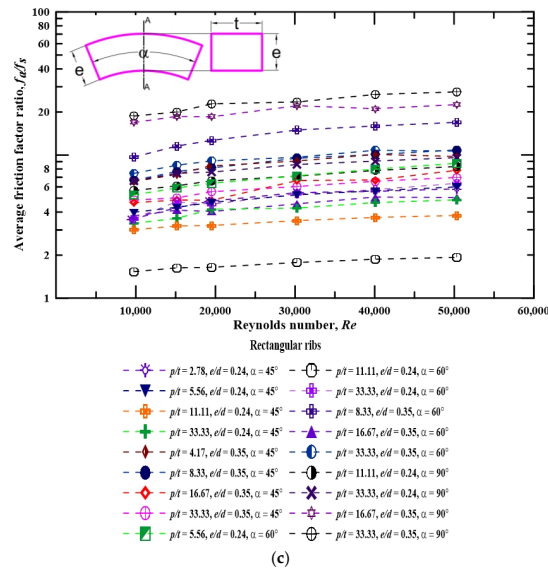
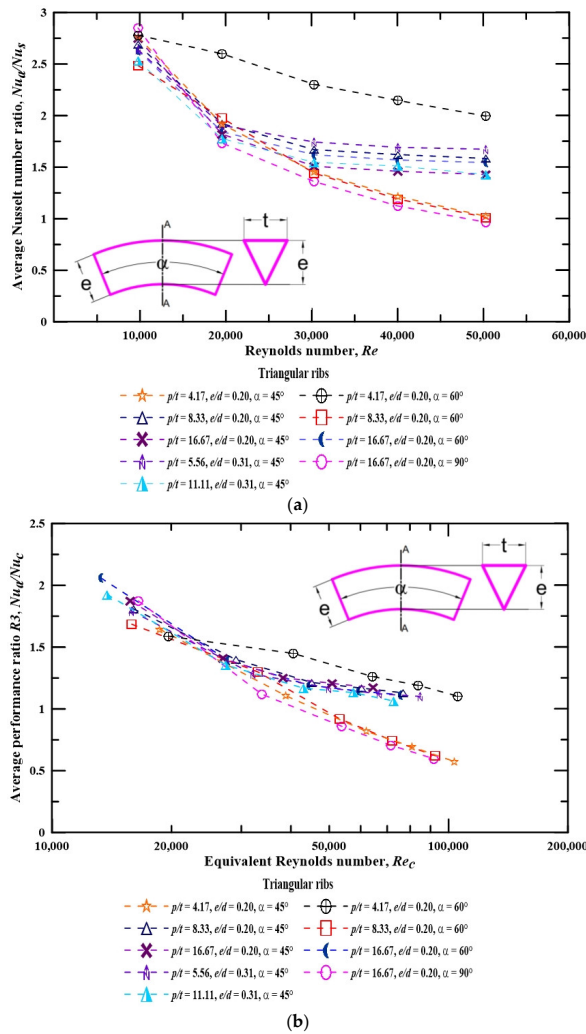


Figure 9. Cont.



**Figure 9.** Experimental results for rectangular ribs variation in (a) average enhancement ratio  $Nu_a/Nu_s$  with Reynolds number  $Re$ ; (b) average performance factor  $R3$ , i.e.,  $Nu_a/Nu_c$  with equivalent Reynolds number  $Re_c$ ; (c) average friction-factor ratio  $f_a/f_s$  with Reynolds number  $Re$ .



**Figure 10.** Cont.

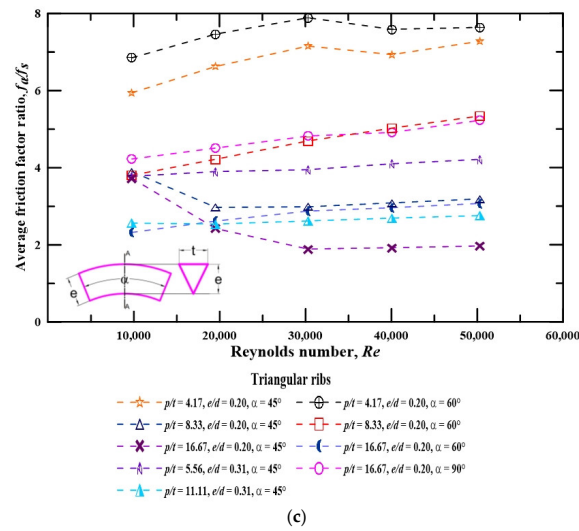


**Figure 10.** Experimental results for triangular ribs variation in (a) average enhancement ratio  $Nu_a/Nu_s$  with Reynolds number  $Re$ ; (b) average performance factor  $R3$ , i.e.,  $Nu_a Nu_c$  with equivalent Reynolds number  $Re_c$ ; (c) average friction-factor ratio  $f_a/f_s$  with Reynolds number  $Re$ .

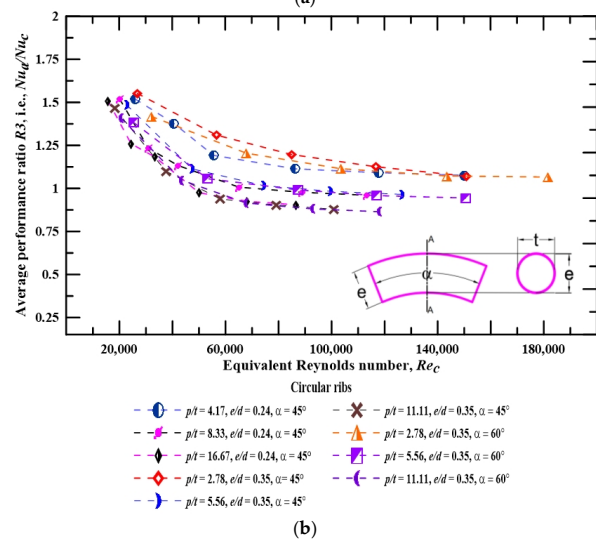
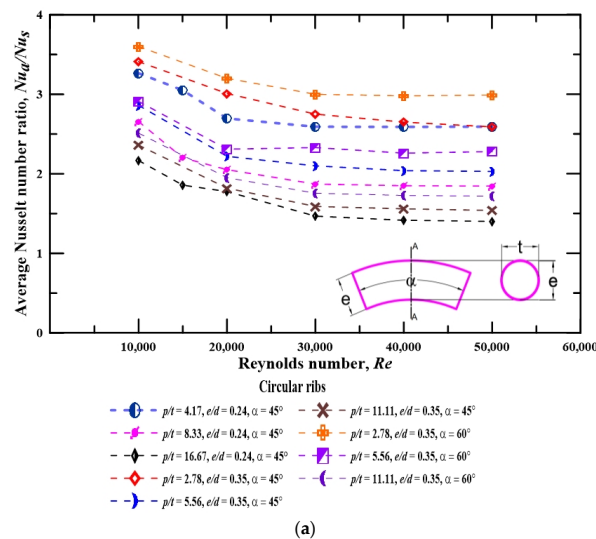


**Figure 11.** Cont.

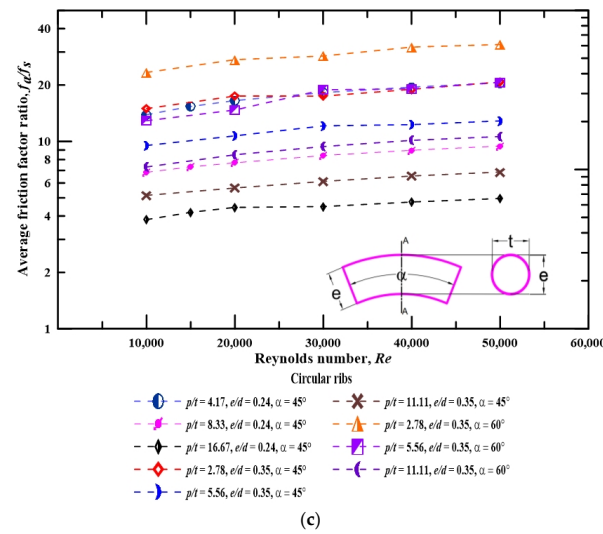


**Figure 11.** Experimental results for circular ribs variation in (a) average enhancement ratio  $Nu_a/Nu_s$  with Reynolds number  $Re$ ; (b) average performance factor  $R3$ , i.e.,  $Nu_a/Nu_c$  with equivalent Reynolds number  $Re_c$ ; (c) average friction-factor ratio  $f_a/f_s$  with Reynolds number  $Re$ .

It is also observed that friction-factor enhancement remains constant with the variation in Reynolds number for a particular rib configuration. Figure 11c shows the change in the average performance factor  $R3$ , i.e.,  $Nu_a/Nu_c$  for different configurations of circular ribs for different  $p/t$  ratios, contact angle  $\alpha$ , and  $e/d$  ratios. It is observed that the performance of circular ribs is observed to be high at lower values of equivalent Reynolds number until reaching 40,000; beyond this value, this factor is reduced and remains constant with equivalent Reynolds number. The general observation for all rib configurations is that the rib elements with a higher contact angle  $\alpha$  and at a low pitch-to-rib thickness  $p/t$  ratio offer more frictional resistance to fluid flow. This high frictional resistance is due to the relatively greater fluid contact with the solid surface of the curved ribs. The square and triangular curved rib elements caused less friction-factor enhancement than the rectangular and circular curved rib elements because the lower surface area was exposed to the flowing fluid. Also, there is a linear decrease in the performance factor  $R3$  value with respect to the equivalent Reynolds number  $Re_c$ . Interestingly, the performance factor  $R3$  is between 1.5 and 2.65 to a  $Re_c$  value of 20,000. Therefore, it is essential to conclude that the rib configurations are suitable at lower flow rates. After that, the performance factor  $R3$  linear value drops and reaches 1.0, or even less, for a few configurations.

#### 4. Design of ANN Architecture

The dataset taken for the prediction is of curved ribs used in the mechanical engineering domain. The training dataset consisted of parameters such as the Reynolds number,  $p/b$ ,  $e/d$ , and beta as the dependent variables and  $Nua/Nus$ ,  $Nua/Nuc$ , and  $f_a/f_s$  as the independent variables. The dataset was trained on the dependent variables and one independent variable at a time, validated, and inferenced, recording the metrics at the same time. The regression analysis uses ANN to predict the Nusselt number ratio  $Nua/Nus$ , friction-factor ratio  $f_a/f_s$ , and performance ratio  $R3$ , i.e., Nusselt number ratio  $Nua/Nuc$  at the same pumping power.

##### 4.1. ANN Intuition

The ANNs, usually called neural networks or neural nets [31], are computing systems inspired by the biological neural networks that constitute the natural brain [32]. Similar to a neural network inside the brain, there are interconnected neurons. These collections of the connected nodes inside the network are called neurons. Each artificial neuron has inputs and produces a single output that can be sent to multiple other neurons [33]. Along

with multiple inputs, each neuron has an activation function. Activation functions shape the outputs of artificial neurons and are integral parts of neural networks in general and deep learning in particular. Some activation functions, such as logistics and ReLU, have been used for decades [34]. These activation functions are equations of the weighted sum of the outputs given by the previous neurons. Further, a bias is added to the sum to form a complete equation.

#### 4.2. Hyperparameters

Hyperparameters dictate the output neuron's result and control the learning process to determine the model parameters that a learning algorithm learns [35]. Standard hyperparameters are explained below.

#### 4.3. Train–Test Split Ratio

The train–test split ratio splits the existing dataset into train and test sets. A proportionate split balance ensures optimal results (generally at 80%:20%). The model is fitted over the training dataset and evaluated over the test dataset. This property checks if the model gives generalised results.

#### 4.4. Learning Rate in Optimisation Algorithms

The learning rate is a hyperparameter that controls how much we adjust our network weights with respect to the loss gradient [36]. As shown in Figure 12, choosing a small value will slow conversion to the minimum, while taking a considerable value can result in missing the minimum [37]. The error intuition is shown in Figure 13.

$$\theta_1 = \theta_1 - \alpha \frac{\partial}{\partial \theta_1} J(\theta_1)$$

*If  $\alpha$  is too small, gradient descent can be slow*

*If  $\alpha$  is too large, gradient descent can overshoot the minimum. It may fail to converge or even diverge.*

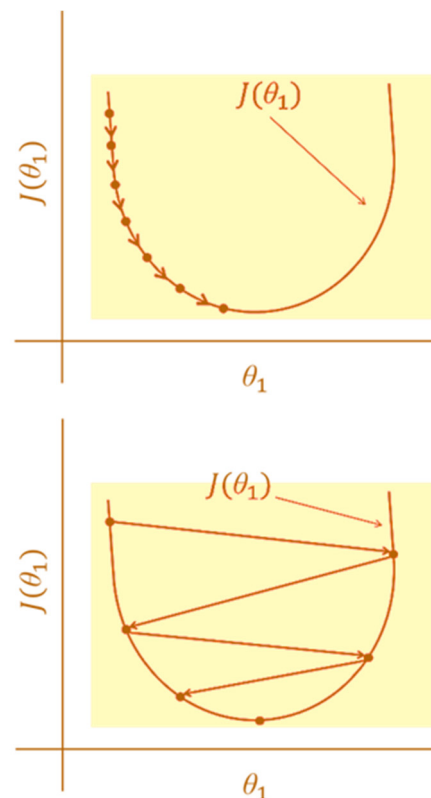


Figure 12. Cost minimisation.

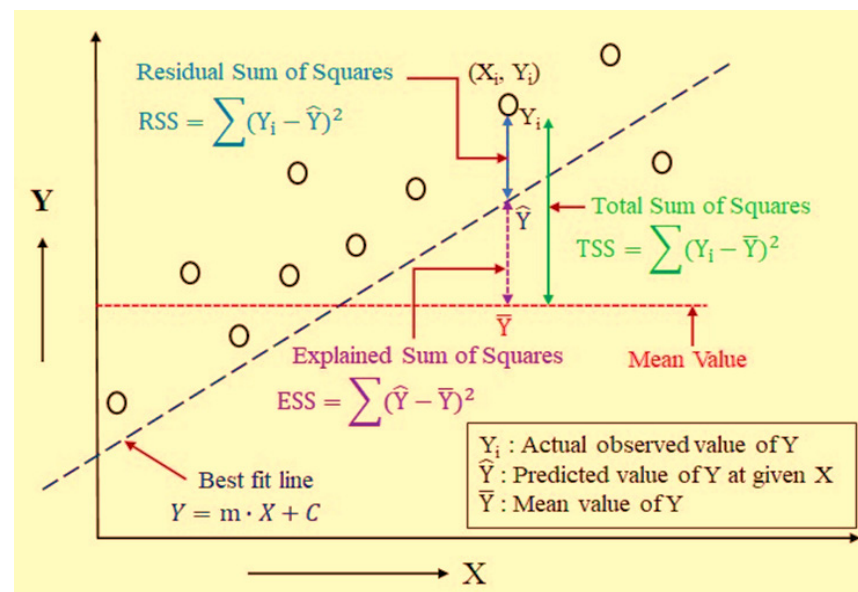


Figure 13. Error intuition.

#### 4.5. Choice of the Optimisation Algorithm

An optimisation algorithm discovers the parameter values attributed to minimising the error for mapping inputs to outputs. These optimisation algorithms widely affect the deep learning model's accuracy [38].

#### 4.6. Choosing of Correct Activation Function

Activation functions control the learning process of learning. An activation function controls the way how a network learns the training dataset. The right choice will help better learn the dataset and generate a generalised model.

#### 4.7. Model-Based Choice of Cost-or-Loss Function

The cost function helps us to find an optimal solution. It is used to evaluate the performance of our model. There are mainly three types of cost functions:

- Regression cost function is mainly used to evaluate regression results where the distance-based error is calculated.
- Classification cost function is mainly used for evaluating results of classification problems such as binary and multiclass classification, where prediction is made between the number of classes in the dataset.
- The correct choice of the cost function for the problem helps to evaluate the model accurately.

#### 4.8. Hidden Layers

The hidden layers in a neural network are located between the input and output layers. Here, the function multiplies the weight of the inputs, generating the output through an activation function. The right choice of the number of neurons results in the model avoiding overfitting or underfitting, and helps the output layer to give an accurate prediction.

#### 4.9. Number of Epochs in Training a Neural Network

In training a neural network, the dataset is passed through the neural network two times, namely the forward pass and the backward pass. One epoch is one forward and one backward pass. The learning process occurs, and the error rate is minimised through the number of epochs. The correct number of epochs helps the network to learn and minimise errors.

#### 4.10. Batch Size

The batch size [39] is designated as the number of examples of training datasets for estimating error gradients. This batch size is an essential hyperparameter as it affects the changing aspects in the learning algorithm. Batch size also limits the accuracy of the error gradient in the training process.

### 5. Machine Learning Results and Discussion

In designing an artificial neural network, parameters affecting the results should be trained and tested on the data. These parameters are tuned over various experimental runs and eventually decided.

#### 5.1. Design and Development of ANN

Initially, the dataset is divided into training and testing datasets (with the split 80:20). Here, the scaling of the data is performed. Standard scaling is carried out on the input variables, as some may have different units and can be distributed inconsistently. Standard scaling helps the model obtain standardised real-valued input and gives a standardised output. The standardised data are input to the neural network's input layer. Then, an optimisation algorithm is used for optimal weight updation. A learning rate is chosen according to the complexity of the model and dataset, which helps minimise the loss function. An activation function is applied to each neuron in the hidden layer to remove the dataset's linearity. The output layer performs neuron activation according to the desired output. To evaluate the model, a loss metric is chosen according to the problem statement.

#### 5.2. Design of Neural Network for a Generalised Prediction

The artificial neural network was built using the TensorFlow-Keras deep learning framework. Two hidden layers have been used with 20 and 10 neurons. Each neuron had normal kernel initialisation and the 'relu' activation function. For the output layer, the 'linear' activation function was used.

#### 5.3. ReLU

This activation function is commonly used as it solves the vanishing gradient problem and converts the loss function with less time complexity. The mathematical equation of ReLU is  $\text{ReLU}(x) = \max(0, x)$ . If the output value is negative, then '0' is considered an output. The graphical representation of the ReLU function is shown in Figure 14. The linear mathematical representation of the linear activation function is  $\text{Linear}(x) = a \cdot x$ , where  $a$  is a constant. The graphical representation of the linear function is shown in Figure 15. The 'Adam' optimiser was used for updating weights, as explained in the next subsection.

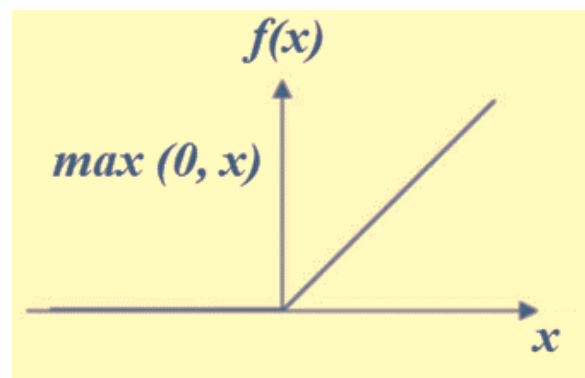
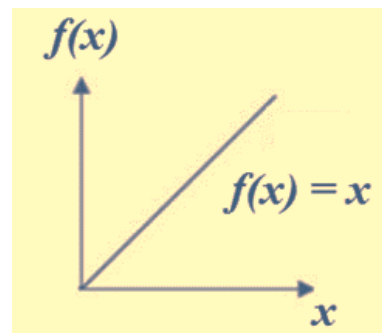


Figure 14. ReLU function.



**Figure 15.** Linear function.

#### 5.4. Adam

A stochastic gradient descent method, known as Adam optimisation, is established on the adaptive approximation of first-order and second-order instances [40]. The metric used to evaluate the model was mean-squared error.

#### 5.5. Mean-Squared Error

Mean-squared error measures the average of squares of errors. In other words, it is a measure of the average squared difference between the estimated values and the actual values.

$$\text{Mean-square error, MSE} = \frac{1}{n} \sum (y - y')^2$$

where  $y$ ,  $y'$ , and  $n$  are the actual value, the predicted value, and the total number of samples, respectively. The neural network was trained over 50 epochs with batch size 64.

#### 5.6. Computational Environment

The system that was used for all the experimentation was Tensorflow-2.8.0 and Keras-2.8.0. GPU support was not taken for experimentation as the CPU operation was possible and computationally light. This environment was used to conduct the experiments and execute the possible choices for the hyperparameters and models.

#### 5.7. Predictions Using Designed ANN and Hyperparameter Tuning

The dataset taken for the prediction is of curved ribs used in the mechanical engineering domain. The training dataset consisted of parameters such as the Reynolds number,  $p/b$ ,  $e/d$ , and beta as the dependent variables and  $Nua/Nus$ ,  $Nua/Nuc$ , and  $fa/fs$  as the independent variables. The dataset was trained on the dependent variables and one independent variable at a time, validated, and inferenced, recording the metrics at the same time. The hyperparameter tuning is explained here.

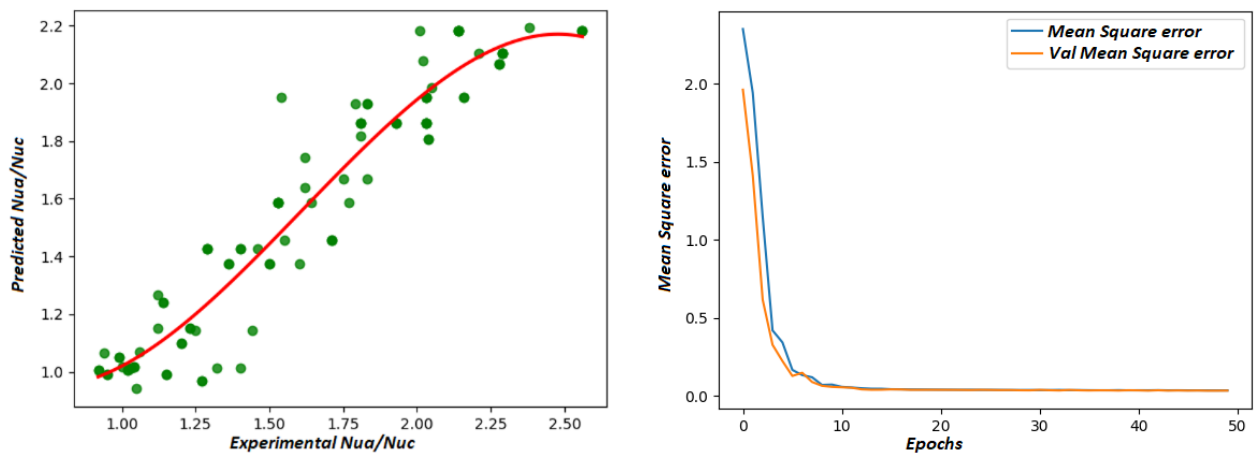
- **Depth:** As the data size after the upsampling was 50 rows, the depth of the neural network was chosen to be 2 instead of 3. The neural network with depth of 3 was overfitting on the dataset and was not providing acceptable results. Thus, a neural network of the depth size of 2 hidden layers was selected.
- **Nodes:** Our experimentation consisted of increasing the node size by a factor of 5. The first hidden layer is responsible for generating accurate results to feed into the next layer for learning purposes; hence, the number of 20 was chosen after trying increments of 5 nodes starting for 5, as it gave a better performance compared to 5, 10, and 15 nodes. For similar reasons, the next hidden layer had 10 nodes. The network ended with a single node for prediction.
- **Learning rate:** The learning rate signifies the learning steps of the pass in the neural network. A learning rate that is too high will make the learning jump over minima, but a learning rate that is too low will either take too long to converge or become stuck

in an undesirable local minimum. For this particular application, the learning rate of 0.01 was chosen, which gave good results and good convergence.

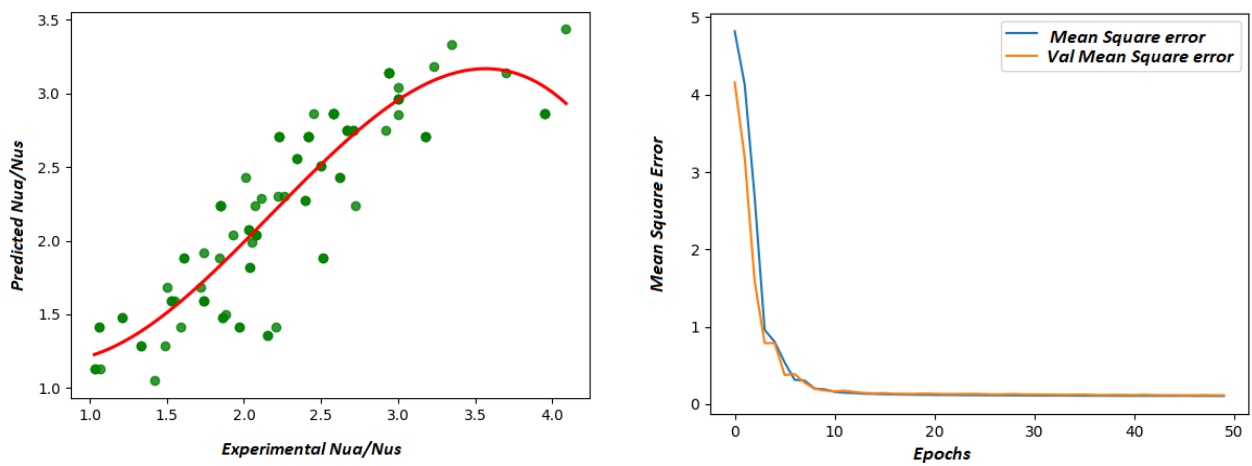
- Activation function: Regression problems solved with artificial neural network use tanh or ReLU as an activation function. For this application, the neural network had a shallow depth; hence, the most appropriate choice of ReLU activation function was applied and good results were obtained.
- Batch size: Batch size signifies the batch of data that passes through a neural network for one cycle of forward and backward pass. For this application, the data size was relatively small so a batch size of 64 was chosen. A lesser batch size would have taken more time to learn; a lower learning rate or higher number of epochs results in more time necessary for convergence.
- Epochs: For the experimentation a value of 50 epochs was most appropriate for the hyperparameter values chosen above. More epochs would have resulted in overfitting and fewer epochs would have resulted in fewer accurate predictions.

All of the hyperparameters values obtained through experimentation were chosen by taking into consideration the minimum convergence of the loss function, which directly signifies better and optimised learning from the algorithm's side, providing better results with each experimentation iteration.

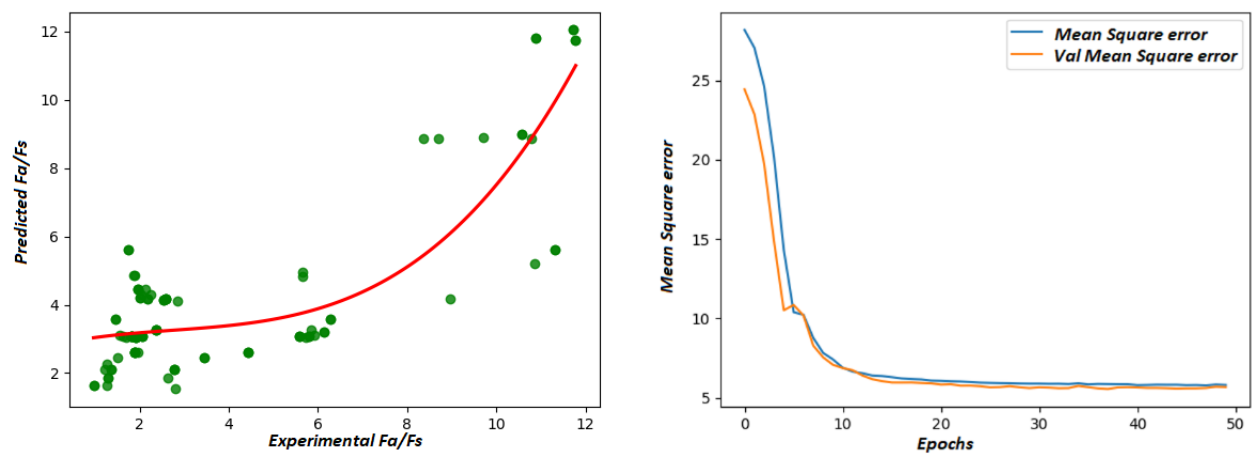
Figure 16 compares the  $Nua/Nuc$ ,  $Nua/Nus$ , and  $fa/ffs$  values between the predicted and actual experimental values for square ribs. It is clear from the figure that a slight variation is observed in the prediction of the ANN model with the experimental values. It is important to note that the performance of the model was observed to be 80% accurate on the tested dataset. A similar variation trend in the predicted and experimental values is observed for rectangular ribs, as shown in Figure 17. However, Figures 18 and 19 show that the comparison of  $Nua/Nuc$ ,  $Nua/Nus$ , and  $fa/ffs$  values with the ANN prediction is observed to be very close to the experimental values for triangular and circular ribs. It is important to note that the performance of the model was observed to be 95% accurate on the tested dataset for these ribs. Accuracy is a metric typically used in classification tasks to measure the percentage of correctly classified instances.  $R^2$ , on the other hand, is a statistical measure designed explicitly for regression analysis. It assesses the goodness of fit in a regression model and indicates the proportion of the variance in the dependent variable that can be explained by the independent variables.  $R^2$  ranges from 0 to 1, where 1 represents a perfect fit and 0 represents no linear relationship. While accuracy is a straightforward measure for classification tasks, it is not directly applicable to regression problems because it focuses on categorical outcomes rather than continuous values. In regression, the goal is to predict and explain the continuous variation in the dependent variable. Therefore, accuracy, which counts correct classifications, does not provide an appropriate evaluation for the performance of regression models.  $R^2$  is commonly used in regression analysis to measure how well the model captures and explains the variance in the data. It indicates the proportion of the dependent variable's variability that can be accounted for by the independent variables. The result submitted where the prediction accuracy is mentioned as 95% is actually the  $R^2$  score obtained on the independent variables in the dataset. The obtained  $R^2$  score was 95% for all dependent variables. This indicates that the ANN model can explain 95% of the total variance observed in the dependent variables based on the information provided by the independent variables. To achieve such high performance, the ANN model has learned the optimal weights and biases through an optimisation algorithm (Adam), which minimises the difference between the predicted values and the actual values of the dependent variables. The model's ability to capture and generalise from the training data enables it to make accurate predictions on unseen data.



(a)

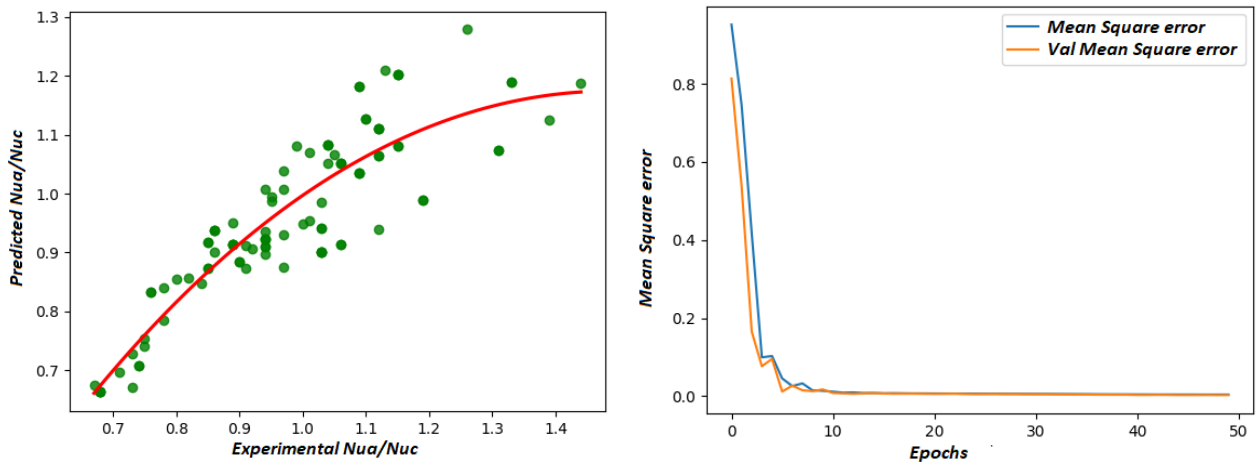


(b)

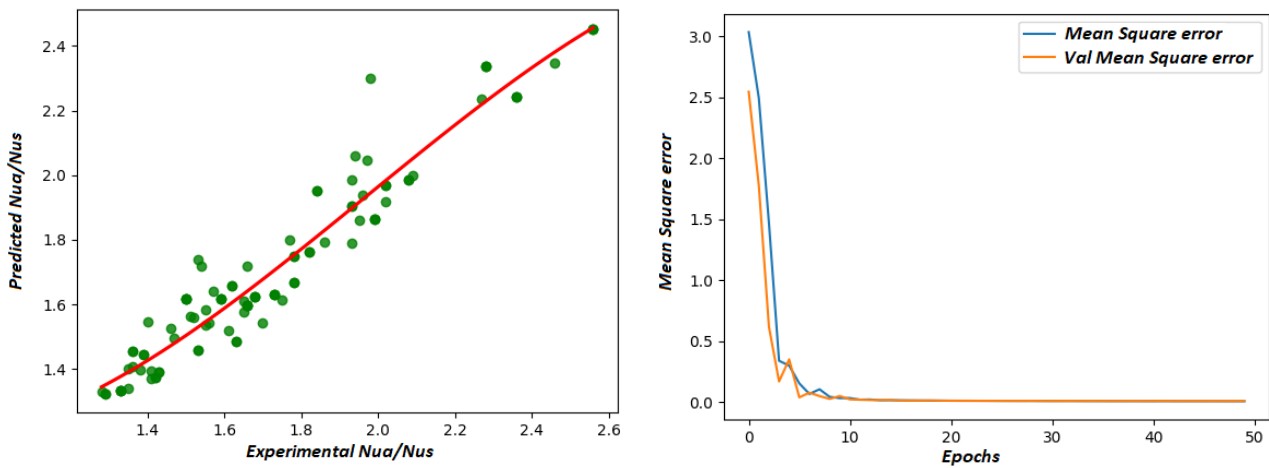


(c)

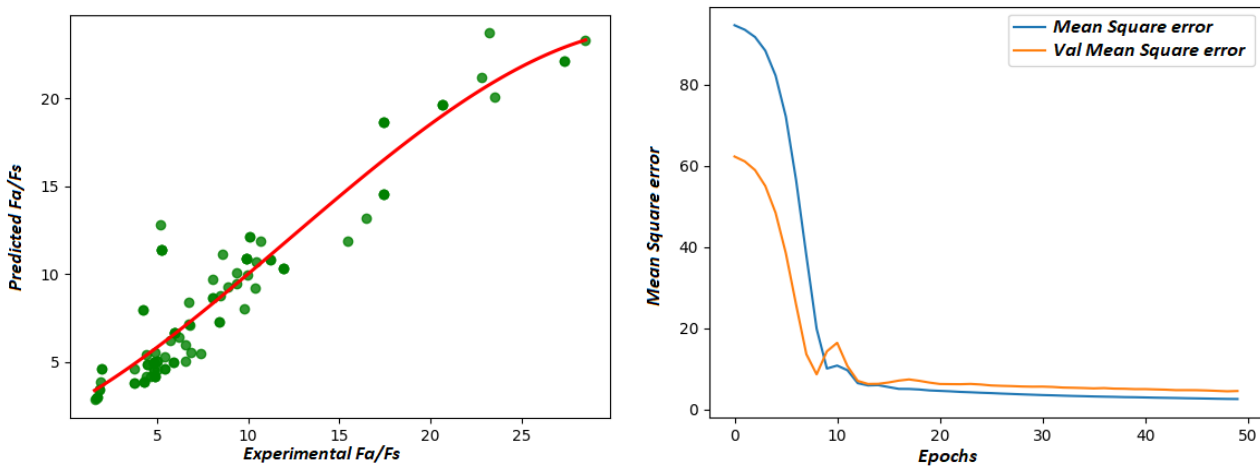
Figure 16. Results for square ribs prediction of (a)  $Nua/Nuc$ , (b)  $Nua/Nus$ , and (c)  $fa/fs$  vs. experimental values and corresponding mean-square error as a function of epochs.



(a)

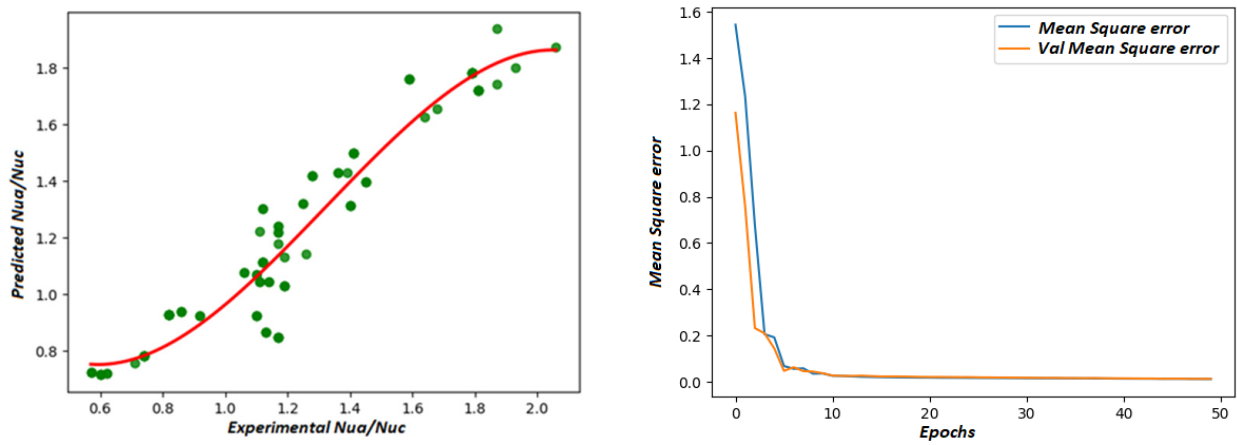


(b)

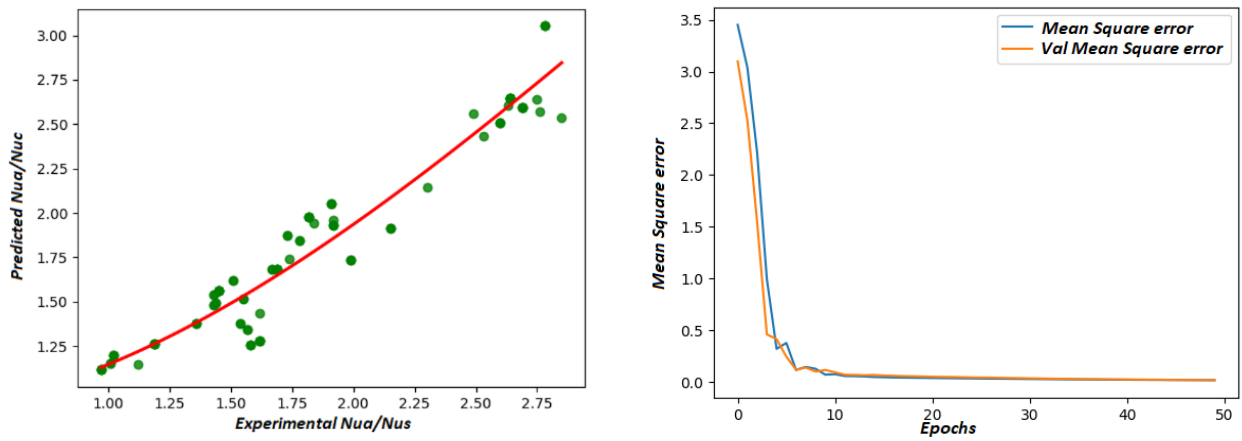


(c)

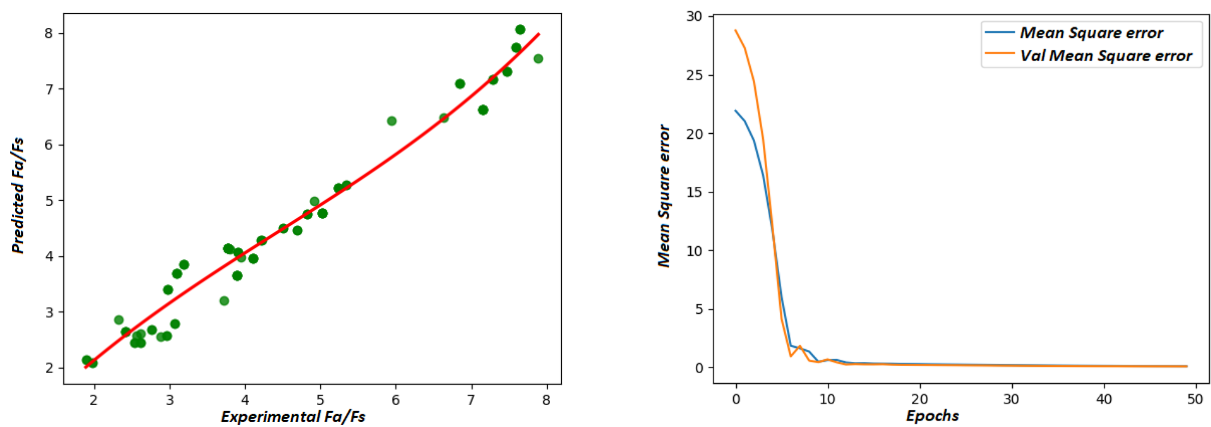
Figure 17. Results for rectangular ribs prediction of (a)  $Nua/Nuc$ , (b)  $Nua/Nus$ , and (c)  $fa/fs$  vs. experimental values and corresponding mean-square error as a function of epochs.



(a)



(b)



(c)

**Figure 18.** Results for triangular ribs prediction of (a)  $Nua/Nuc$ , (b)  $Nua/Nus$ , and (c)  $fa/fs$  vs. experimental values and corresponding mean-square error as a function of epochs.

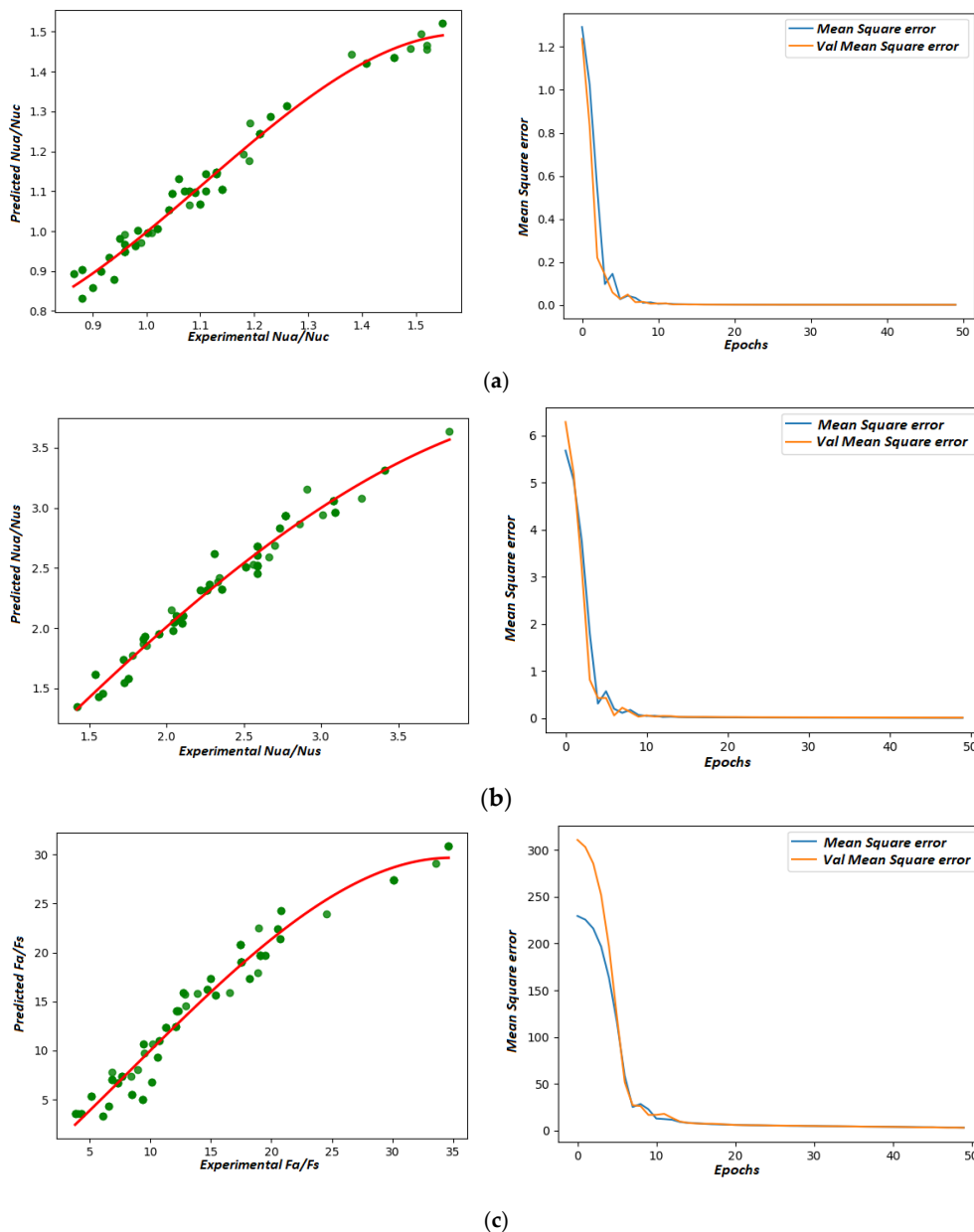


**Figure 19.** Results for circular ribs prediction of (a)  $Nua/Nuc$ , (b)  $Nua/Nus$ , and (c)  $fa/fs$  vs. experimental values and corresponding mean-square error as a function of epochs.

The main aim for employing machine learning techniques in this investigation was to predict and assess the thermohydraulic performance of curved ribs through regression analysis. By leveraging the competence of ML, the pitfalls of conventional experimental and analytical methods, i.e., often resource-intensive and time-consuming and relying on simplifications and assumptions, are overcome and explained herein.

- Enhanced prediction accuracy: ML models revealed tedious patterns and relationships within a dataset of multiple variables, enabling prediction of thermohydraulic performance indicators more accurately. The experimental data were trained and it learned from the involved relations among various factors—the Reynolds number,  $p/b$ ,  $e/d$ , and  $\beta$  as the dependent variables and  $Nua/Nus$ ,  $Nua/Nuc$  and  $fa/fs$  as the independent variables—and provided reliable predictions with high accuracy of 95% for the tested dataset.

- Cost and time efficiency: The conventional experimental approaches often need extensive data collection and testing; however, ML allows for reducing the effort required to collect extensive data through experimentation while still achieving accurate predictions. By training existing data collected through experimentation, prediction of performance indicators without undertaking further time-consuming trials was achieved. This feature expressively reduced the cost and time while assessing numerous configurations of the curved rib.
- Comprehensive performance evaluation: The ML algorithm predicted multiple performance indicators simultaneously, exhibiting an inclusive assessment of various heat transfer enhancement parameters. In this study, the artificial neural network predicted heat transfer indicators providing perceptions into different aspects of curved rib performance using a single modelling approach.
- Identification of optimal rib configurations: Through ML, the configurations of curved rib which showed the highest performance factor  $R3$  at different Reynolds numbers were identified. This inference appears valuable in the design of heat-exchanging devices with curved ribs tailored to particular applications, ensuring optimal heat transfer performance.

## 6. Conclusions

The experimental results are presented to investigate the thermohydraulic performance of ribs used for flow through a circular pipe for turbulent flow conditions. The present study has the following conclusions:

- The average Nusselt number ratio of the tube with ribs to the Nusselt number of the tube without ribs,  $Nua/Nus$ , increases with the Reynolds number,  $Re$ . This trend is observed for all rib types.
- The general observation for all rib configurations is that the rib elements with a higher contact angle value  $\alpha$  and at a low pitch-to-rib thickness  $p/t$  ratio offer more frictional resistance to fluid flow.
- The square and triangular curved rib elements caused less friction-factor enhancement than the rectangular and circular curved rib elements because the lower surface area was exposed to the flowing fluid.
- A linear decrease in the performance factor  $R3$  value was observed for all types of ribs with respect to the equivalent Reynolds number  $Rec$ .
- The best configuration of square ribs produces the value of performance factor  $R3$  in the range of 1.5 to 2.65 until the equivalent Reynolds number  $Rec$  attained a value of 20,000.
- It can be concluded that the rib configurations are suitable at lower flow rates. After that, the performance factor  $R3$  linear value drops and reaches 1.0, or even less, for a few configurations.
- It is important to note that using ribs with different cross sections offers effective alternatives/additional methods for heat transfer enhancement over the other passive methods reported in the literature.
- An ANN model predicts the performance indicators like average heat transfer enhancement  $Nua/Nus$ , average heat transfer enhancement  $fa/fs$ , and performance ratio  $R3$ , i.e.,  $Nua/Nuc$ .
- The models were evaluated to have an accuracy of 95.00% on unknown test data, and the proposed model reasonably forecasted  $Nua/Nus$ ,  $fa/fs$ , and  $Nua/Nuc$ .

**Author Contributions:** Conceptualization, P.D. and S.L.; Methodology, P.D. and A.D.P.; Software, P.D. and H.S.; Validation, P.D., H.S. and A.D.P.; Formal analysis, P.D., H.S. and A.D.P.; Investigation, P.D., S.L., A.D.P. and S.G.; Resources, S.L. and S.G.; Writing—original draft, P.D., S.L. and H.S.; Writing—review & editing, P.D. and A.D.P.; Visualization, P.D., A.D.P. and S.G.; Supervision, S.L. and S.G.; Project administration, S.L. and S.G. All authors have read and agreed to the published version of the manuscript.

**Funding:** This research received no external funding.

**Data Availability Statement:** Data are available on request.

**Conflicts of Interest:** The authors declare no conflict of interest.

## Nomenclature

$A$	inside surface area of the circular tube ( $\pi dL$ ), $m^2$
$t$	rib thickness, $m$
$C_p$	specific heat at constant pressure, $J/kg.K$
$d$	inner diameter of the tube, $m$
$e$	height of the rib element, $m$
$e/d$	ratio of rib height to inner tube diameter, dimensionless
$f$	friction factor, dimensionless
$f_a$	friction factor for the tube fitted with curved ribs, i.e., enhanced tube, dimensionless
$f_s$	friction factor for the smooth tube, i.e., tube without any ribs, dimensionless
$L$	length of the test section, $m$
$\dot{m}$	mass flow rate of the fluid, $kg/s$
$Nu$	Nusselt number, dimensionless
$Nu_a$	Nusselt number for the tube fitted with curved ribs, i.e., enhanced tube, $\left(= \frac{\rho.v.d}{\mu}\right)$
$Nu_s$	Nusselt number for the smooth tube, i.e., tube without ribs, $\left(= \frac{\rho.v.d}{\mu}\right)$
$Nuc$	Nusselt number for the equivalent smooth tube, i.e., the tube without curved ribs runs at the same pumping power as that of the enhanced tube,
$p$	pitch of rib configuration, $m$
$p/t$	ratio of the pitch to rib thickness
$Pr$	Prandtl number $\left(= \frac{\mu.C_p}{\Gamma}\right)$
$Q_{out}$	heat transfer rate to the flowing fluid between the inlet and outlet, $W$
$\dot{q}$	constant heat flux, $W/m^2$
$Re$	Reynolds number, $\left(= \frac{\rho.v.d}{\mu}\right)$
$Re_a$	Reynolds number for the tube fitted with curved ribs, i.e., enhanced tube, $\left(= \frac{\rho.v.d}{\mu}\right)$
$Re_s$	Reynolds number for the smooth tube, i.e., tube without curved ribs, $\left(= \frac{\rho.v.d}{\mu}\right)$
$Re_c$	Reynolds number for the smooth tube at the same pumping power as that of the tube fitted with curved ribs, i.e., enhanced tube, $\left(= \frac{\rho.v.d}{\mu}\right)$
$T$	temperature, $K$
$T_{bi}$	bulk temperature of the fluid at the inlet of the tube, $K$
$T_{bo}$	bulk temperature of the fluid at the outlet of the tube, $K$
$T_W$	temperature of the inner wall of the tube, $K$
$v$	average fluid velocity, $m/s$

## Greek Symbols

$k$	thermal conductivity of the fluid, $W/m.K$
$\alpha$	included angle of the rib element, $^\circ$
$\mu$	dynamic viscosity, $Pa.s$
$\rho$	fluid density, $kg/m^3$
$\Delta P$	pressure drop between inlet and outlet of the test section, $N/m^2$

## Subscripts

$b$	bulk fluid
$a$	augmented tube
$s$	smooth tube flow at the equal Reynolds number
$c$	smooth tube flow at the equal pumping power
$w$	tube wall

## References

1. Koşar, A.; Peles, Y. Convective flow of refrigerant (R-123) across a bank of micro pin fins. *Int. J. Heat Mass Transf.* **2006**, *49*, 3142–3155. [[CrossRef](#)]
2. Ma, X.; Sha, J.; Wang, D.; Yu, Y.; Yang, Q.; Niu, X. Study on a prediction of P2P network loan default based on the machine learning LightGBM and XGboost algorithms according to different high dimensional data cleaning. *Electron. Commer. Res. Appl.* **2018**, *31*, 24–39. [[CrossRef](#)]

3. Mei, D.; Lou, X.; Qian, M.; Yao, Z.; Liang, L.; Chen, Z. Effect of tip clearance on the heat transfer and pressure drop performance in the micro-reactor with micro-pin-fin arrays at low Reynolds number. *Int. J. Heat Mass Transf.* **2014**, *70*, 709–718. [[CrossRef](#)]
4. Duangthongsuk, W.; Wongwises, S. A comparison of the heat transfer performance and pressure drop of nanofluid-cooled heat sinks with different miniature pin fin configurations. *Exp. Therm. Fluid Sci.* **2015**, *69*, 111–118. [[CrossRef](#)]
5. Jeng, T.-M.; Tzeng, S.-C. Pressure drop and heat transfer of square pin-fin arrays in in-line and staggered arrangements. *Int. J. Heat Mass Transf.* **2007**, *50*, 2364–2375. [[CrossRef](#)]
6. Lee, H.; Kang, M.; Jung, K.W.; Kharangate, C.R.; Lee, S.; Iyengar, M.; Malone, C.; Asheghi, M.; Goodson, K.E.; Lee, H. An artificial neural network model for predicting frictional pressure drop in micro-pin fin heat sink. *Appl. Therm. Eng.* **2021**, *194*, 117012. [[CrossRef](#)]
7. Yang, L.; Wang, Q.; Rao, Y. Searching for irregular pin-fin shapes for high temperature applications using deep learning methods. *Int. J. Therm. Sci.* **2020**, *161*, 106746. [[CrossRef](#)]
8. Kang, M.S.; Park, S.G.; Dinh, C.T. Heat transfer enhancement by a pair of asymmetric flexible vortex generators and thermal performance prediction using machine learning algorithms. *Int. J. Heat Mass Transf.* **2023**, *200*. [[CrossRef](#)]
9. Kim, S.-K.; Huh, J.-H. Consistency of Medical Data Using Intelligent Neuron Faster R-CNN Algorithm for Smart Health Care Application. *Healthcare* **2020**, *8*, 185. [[CrossRef](#)]
10. Cho, E.; Lee, H.; Kang, M.; Jung, D.; Lee, G.; Lee, S.; Lee, H. A neural network model for free-falling condensation heat transfer in the presence of non-condensable gases. *Int. J. Therm. Sci.* **2022**, *171*, 107202. [[CrossRef](#)]
11. Kim, K.; Lee, H.; Kang, M.; Lee, G.; Jung, K.; Kharangate, C.R.; Asheghi, M.; Goodson, K.E.; Lee, H. A machine learning approach for predicting heat transfer characteristics in micro-pin fin heat sinks. *Int. J. Heat Mass Transf.* **2022**, *194*, 123087. [[CrossRef](#)]
12. Gau, C.; Lee, C. Impingement cooling flow structure and heat transfer along rib-roughened walls. *Int. J. Heat Mass Transf.* **1992**, *35*, 3009–3020. [[CrossRef](#)]
13. Talapati, R.; Katti, V. Influence of turbulator under the detached rib on heat transfer study of air jet impinging on a flat surface. *Int. J. Therm. Sci.* **2023**, *184*, 107946. [[CrossRef](#)]
14. Chuwattanakul, V.; Wongcharee, K.; Ketain, P.; Chamoli, S.; Thianpong, C.; Eiamsa-Ard, S. Aerothermal performance evaluation of a tube mounted with broken V-ribbed twisted tape: Effect of forward/backward arrangement. *Case Stud. Therm. Eng.* **2023**, *41*, 102642. [[CrossRef](#)]
15. He, Q.; Zhao, W.; Chi, Z.; Zang, S. Application of deep-learning method in the conjugate heat transfer optimization of full-coverage film cooling on turbine vanes. *Int. J. Heat Mass Transf.* **2022**, *195*, 123148. [[CrossRef](#)]
16. Boonloi, A.; Jedsadaratanachai, W. Numerical predictions of flow topology and heat transfer in a square duct with staggered V-ribs. *Int. Commun. Heat Mass Transf.* **2022**, *139*, 106483. [[CrossRef](#)]
17. Lee, Y.J.; Lee, P.S.; Chou, S.K. Enhanced Thermal Transport in Microchannel Using Oblique Fins. *J. Heat Transf.* **2012**, *134*, 101901. [[CrossRef](#)]
18. Guan, N.; Jiang, G.; Liu, Z.G.; Zhang, C.W. Effects of heating load on flow resistance and convective heat transfer in micro-pin-fin heat sinks with different cross-section shapes. *Exp. Heat Transf.* **2014**, *29*, 673–690. [[CrossRef](#)]
19. Hua, J.; Li, G.; Zhao, X.; Li, Q. Experimental study on thermal performance of micro pin fin heat sinks with various shapes. *Heat Mass Transf.* **2016**, *53*, 1093–1104. [[CrossRef](#)]
20. Kharangate, C.R.; Jung, K.W.; Jung, S.; Kong, D.; Schaadt, J.; Iyengar, M.; Malone, C.; Lee, H.; Asheghi, M.; Goodson, K.E. Experimental Investigation of Embedded Micropin-Fins for Single-Phase Heat Transfer and Pressure Drop. *J. Electron. Packag.* **2018**, *140*, 021001. [[CrossRef](#)]
21. Hou, F.; Yang, D.; Zhang, G.; Hai, Y.; Liu, D.; Liu, L. Thermal transient analysis of LED array system with in-line pin fin heat sink. In Proceedings of the 12th International Conference on Thermal, Mechanical & Multi-Physics Simulation and Experiments in Microelectronics and Microsystems, Linz, Austria, 18–20 April 2011; pp. 1–5. [[CrossRef](#)]
22. Koroleva, A.P.; Kuzmenkov, N.V.; Frantuzov, M.S. Application of machine learning methods for investigating the heat transfer enhancement performance in a circular tube with artificial roughness. *J. Phys. Conf. Ser.* **2020**, *1675*, 012008. [[CrossRef](#)]
23. Kwon, B.; Ejaz, F.; Hwang, L. Machine learning for heat transfer correlations. *Int. Commun. Heat Mass Transf.* **2020**, *116*, 104694. [[CrossRef](#)]
24. Khorunzhii, I.; Gabor, H.; Job, R.; Fahrner, W.R.; Baumann, H. Modelling of a pin-fin heat converter with fluid cooling for power semiconductor modules. *Int. J. Energy Res.* **2003**, *27*, 1015–1026. [[CrossRef](#)]
25. Bayer, S.; Oskouei, B.; Aradag, S. Investigation of double-layered wavy microchannel heatsinks utilizing porous ribs with artificial neural networks. *Int. Commun. Heat Mass Transf.* **2022**, *134*, 105984. [[CrossRef](#)]
26. Panda, J.P.; Kumar, B.; Patil, A.K.; Kumar, M. Machine learning assisted modeling of thermo-hydraulic correlations for heat exchangers with twisted tape inserts. *Int. Commun. Heat Mass Transf.* **2022**; to be submitted.
27. Dittus, F.W.; Boelter, L.M.K. Heat transfer in automobile radiators of the tubular type. *Int. Commun. Heat Mass Transf.* **1930**, *12*, 3–22. [[CrossRef](#)]
28. Moffat, R.J. Describing the uncertainties in experimental results. *Exp. Therm. Fluid Sci.* **1988**, *1*, 3–17. [[CrossRef](#)]
29. Garcia, A.; Vicente, P.G.; Viedma, A. Experimental Study of heat transfer enhancement with wire coil inserts in laminar-turbulent regimes at different Prandtl numbers. *Int. J. Heat Mass Transf.* **2005**, *48*, 4640–4651. [[CrossRef](#)]
30. Zhang, Y.F.; Li, F.Y.; Liang, Z.M. Heat Transfer in Spiral Coil Inserted tubes and its applications. In *Advances in Heat Transfer Augmentation*; Ebadian, M.A., Pepper, D.W., Diller, T., Eds.; ASME Symposium: New York, NY, USA, 2022; Volume HTD 169, pp. 31–36.
31. Larry, H. *Explained: Neural Networks*; Massachusetts Institute of Technology News Office: Cambridge, MA, USA, 2017.

32. Yang, Z.R.; Yang, Z. Artificial Neural Networks. In *Comprehensive Biomedical Physics*; Elsevier: Stockholm, Sweden, 2014; pp. 1–17. ISBN 978-0-444-53633-4.
33. Abbod, M.F.; Catto, J.W.; Linkens, D.A.; Hamdy, F.C. Application of Artificial Intelligence to the Management of Urological Cancer. *J. Urol.* **2007**, *178*, 1150–1156. [[CrossRef](#)]
34. Lederer, J. Activation Functions in Artificial Neural Networks: A Systematic Overview. *arXiv* **2021**, arXiv:2101.09957. [[CrossRef](#)]
35. Nyuytimbiy, K. Parameters & Hyperparameters in Machine Learning. *Towards Data Sci.* **2020**. Available online: <https://towardsdatascience.com/parameters-and-hyperparameters-aa609601a9ac> (accessed on 20 April 2023).
36. Zulkifli, H. Understanding Learning Rates and How It Improves Performance in Deep Learning. *Towards Data Sci.* **2018**. Available online: <https://towardsdatascience.com/understanding-learning-rates-and-how-it-improves-performance-in-deep-learning-d0d4059c1c10> (accessed on 20 April 2023).
37. Gupta, A. A Comprehensive Guide on Optimizers in Deep Learning. 2021. Available online: <https://www.analyticsvidhya.com/blog/2021/10/a-comprehensive-guide-on-deep-learning-optimizers/> (accessed on 21 April 2023).
38. Brownlee, J. How to Control the Stability of Training Neural Networks with the Batch Size. 2019. Available online: <https://machinelearningmastery.com/how-to-control-the-speed-and-stability-of-training-neural-networks-with-gradient-descent-batch-size/> (accessed on 22 April 2023).
39. Shah, T. About train, validation and test sets in Machine Learning. *Towards Data Sci.* **2017**. Available online: <https://towardsdatascience.com/train-validation-and-test-sets-72cb40cba9e7> (accessed on 23 April 2023).
40. Kingma, D.P.; Ba, J. Adam: A Method for Stochastic Optimization. *arXiv* **2014**, arXiv:1412.6980. [[CrossRef](#)]

**Disclaimer/Publisher’s Note:** The statements, opinions and data contained in all publications are solely those of the individual author(s) and contributor(s) and not of MDPI and/or the editor(s). MDPI and/or the editor(s) disclaim responsibility for any injury to people or property resulting from any ideas, methods, instructions or products referred to in the content.